Post-synthesis Oxidation of Superparamagnetic Iron Oxide Nanoparticles to Enhance Magnetic Particle Imaging (MPI) Performance

Authors:

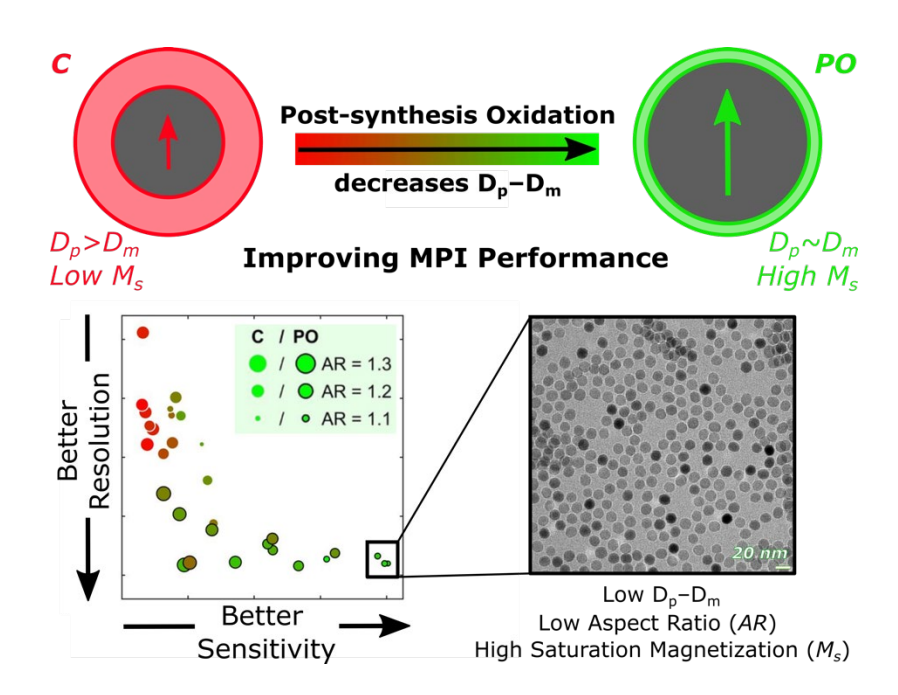
Ambar C. Velazquez-Albino¹, Aniela Nozka², Andrii Melnyk¹, Hayden J. Good¹, Carlos M. Rinaldi-Ramos^{1,3,+}

Affiliations:

- 1. Department of Chemical Engineering, University of Florida, Gainesville, FL 32611
- 2. Department of Bioengineering, Clemson University, Clemson, SC 29634
- 3. J. Crayton Pruitt Family Department of Biomedical Engineering, University of Florida, Gainesville, FL 32611-6131

⁺Corresponding author

TOC



Abstract

This study investigates the impact of post-synthesis oxidation on the performance of superparamagnetic iron oxide nanoparticles (SPIONs) in magnetic particle imaging (MPI), an emerging technology with applications in diagnostic imaging and theranostics. SPIONs synthesized from iron oleate were subjected to a post-synthesis oxidation treatment with a 1% Oxygen in Argon mixture. MPI performance, gauged via signal intensity and resolution using a MOMENTUM™ scanner, was correlated to the nanoparticles' physical and magnetic properties. Post-synthesis oxidation did not alter physical attributes like size and shape, but significantly enhanced magnetic properties. Saturation magnetization increased from 52% to 93% of the bulk value for magnetite, leading to better MPI performance in terms of signal intensity and resolution. However, the observed MPI performance did not fully align with predictions based on the ideal Langevin model, indicating the need for considering factors like relaxation and shape anisotropy. The findings underscore the potential of post-synthesis oxidation as a method to fine-tune magnetic properties of SPIONs and improve MPI performance, and the need for reproducible synthesis methods that afford finely tuned control of nanoparticle size, shape, and magnetic properties.

Keywords: magnetic particle imaging, magnetic nanoparticles, iron oxide, post-synthesis oxidation, thermal annealing, magnetic diameter, saturation magnetization, relaxation

Iron oxide nanoparticles have tremendous potential as magnetic particle imaging (MPI) tracers, with applications in diagnostic imaging and theranostics. PPI can generate 3D images with high spatial and temporal resolution, allowing for visualization of the tracer's distribution in biological environments. MPI signal is derived from the nonlinear response of magnetic iron oxide nanoparticle tracers to an alternating magnetic

field (AMF). Superimposed in the field of view (FOV) is a selection field gradient created by opposing magnets, which generates the field free region (FFR). Only tracers in the FFR respond strongly to the AMF, giving rise to the MPI signal that is mapped in space to produce an image. This renders MPI an ideal method for non-invasive quantitative imaging as the signal generated is directly proportional to the tracer's mass, providing high sensitivity and millimeter-scale resolution. Due to the nature of signal generation in MPI, solely from the tracer's magnetic response, this imaging modality results in negligible tissue and background attenuation, as well as no tissue penetration limitations. These are clear advantages over other imaging modalities to track nanoparticles, such as magnetic resonance imaging (MRI) and fluorescence imaging.⁷

There are currently two main modes of image reconstruction in MPI: harmonic space reconstruction and x-space reconstruction. 1, 23-25 Bruker, in partnership with Phillips, has commercialized pre-clinical harmonic space reconstruction MPI scanners, while Magnetic Insight, Inc., has commercialized pre-clinical x-space reconstruction MPI scanners. There are also several groups developing prototype scanners according to these reconstruction modalities and others under development. The current tracer sold by Magnetic Insight for use in their MOMENTUM MPI scanner is VivoTrax M, a form of ferucarbotran, which was originally developed for use as an MRI contrast agent. VivoTrax Plus is an improved MPI tracer obtained by separating the larger sized nanoparticles in VivoTrax Plus Tailoring tracers to improve MPI performance is crucial to fully maximize this imaging modality's potential. And 30-36 This need for specialized tracers motivates work to synthesize new MPI tracers with varied size, shape, and composition. Resolution specifically is a bottleneck for scale-up of MPI scanners and specific clinical applications. Optimized tracers with higher sensitivity and improved resolution would also reduce costs of clinical MPI scanners by allowing the use of lower magnetic field gradients to achieve the same signal generation.

The point spread function (PSF) is used to characterize MPI tracer performance.^{23, 24} The PSF can be obtained from relaxometry measurements, using the RELAXTM module in the MOMENTUMTM scanner or using custom built magnetic particle susceptometers^{25, 37-39} or relaxometers.^{27, 37, 40-45} Because the signal in MPI is related to the time-derivative of the particle's magnetization response, one can obtain simple relations for the sensitivity (peak intensity, I, of the PSF) and resolution (full width at half maximum, FWHM, of the PSF) by assuming superparamagnetic behavior described by the Langevin function:²⁴

$$I = \frac{NM_S\pi D^3}{18} \,, \tag{1}$$

$$FWHM = \frac{24 \, k_B T}{\mu_0 \pi \, G \, M_s \, D^3}. \tag{2}$$

Here, N is the number density of magnetic nanoparticles (particles/m³), M_s is the saturation magnetization, D is the diameter, k_B is Boltzmann's constant, T is the temperature, μ_0 is the vacuum permeability, and G is the magnetic field gradient strength. Equations (1) and (2) further assume that there are no magnetic interactions between tracers and that magnetization responds instantaneously to the applied field (there are no finite relaxation effects).

While simplistic, equations (1) and (2) have served as guides in the development of MPI tracers. Optimization of tracers tailored for MPI consists of increasing signal intensity (I) and reducing FWHM. Theoretically, from equations (1) and (2), this should be achieved by increasing tracer diameter (D) and saturation magnetization (M_s). Increasing tracer size to improve performance also increases relaxation time, therefore limiting the diameter range for which equations (1) and (2) apply. The saturation magnetization is related to the composition of the tracer, but typical experimental values are lower than those of the corresponding bulk material, and this is often explained by what has been called the "magnetically dead layer," arising due to spin canting and other surface phenomena causing disorder of magnetic dipoles. Furthermore, saturation magnetization is affected by the nanoparticle crystallinity and phase purity, which studies have shown to control through modifications of synthesis conditions. $^{34, 50-52}$

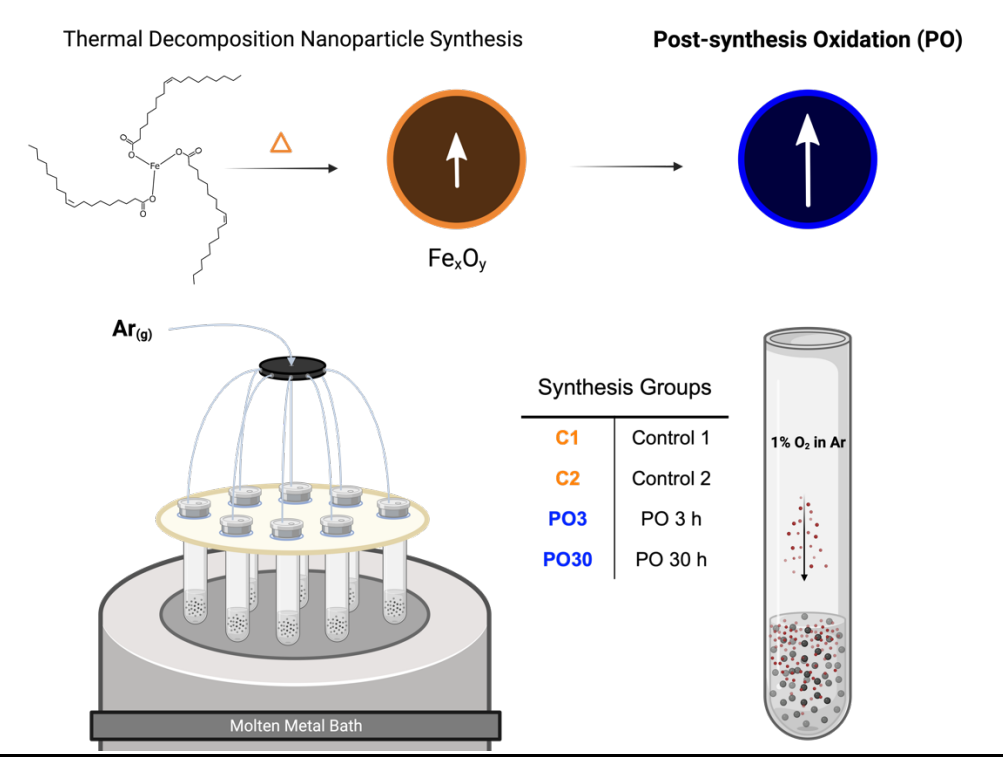
Recent development of MPI tracers have focused on studying superparamagnetic nanoparticles of various sizes, shapes, and compositions.^{15, 16, 20, 21, 27, 28, 38, 39, 42-45, 53-64} Thus far, tracers with the best MPI performance have been synthesized via thermal decomposition, the synthesis method of choice for applications that require fine control over nanoparticle size, shape, and properties. The best tracer reported, LS-1, a 26 nm spherical

single core iron oxide had three times better sensitivity than the commercial tracer Resovist and improved resolution of 1.7 mm in x-space MPI. 27 LS-1 was synthesized by a thermal decomposition method followed by post-synthesis oxidation. This makes sense, given that other studies have demonstrated that oxygen exposure, during or after synthesis, plays a crucial role in magnetic properties of iron oxide nanoparticles. $^{27, 50, 51}$

Here we evaluate the effect of post-synthesis oxidation on the thermal decomposition synthesis of iron oxide nanoparticles intended for use as magnetic particle imaging (MPI) tracers. Physical and magnetic properties are reported and correlated to MPI performance, probing agreement to the Langevin model. Post-synthesis oxidation consistently improved magnetic properties and MPI performance, although there were deviations from the predictions of the Langevin model. It was observed that shape anisotropy and discrepancy between physical and magnetic diameters significantly hinder MPI performance. Statistical analyses were used to evaluate which tracer properties have the greatest impact on MPI performance.

Results

Iron oxide nanoparticles were synthesized via thermal decomposition of iron oleate and with a post-synthesis oxidation treatment to evaluate its effect on nanoparticle physical and magnetic properties and their MPI performance. Recognizing the possibility of variation in nanoparticle properties, something that is not widely reported in the literature but known to researchers in the field, we sought to perform multiple syntheses under each condition to apply statistical analysis in making these comparisons. This motivated us to design a synthesis setup that can carry out 8 simultaneous reactions in a molten metal bath to allow 8 replicates to be synthesized under each synthesis condition (Scheme 1). A replicate of the control group was used to validate our design by showing reproducibility between sets of syntheses synthesized under the same conditions. Two groups of post-synthesis oxidation treatment were used to evaluate the effect of post-synthesis oxidation duration. We will use the following nomenclature for the synthesis conditions tested: C1 for the first control group, C2 for the second control group, PO3 for the 3-hour post-synthesis oxidation group, and PO30 for the 30-hour post-synthesis oxidation group. One replicate of each of the C1 and PO3 groups was eliminated from the study due to sample loss during processing. Ordinary one-way ANOVA statistical analysis was used to compare the means of various physical, magnetic, and MPI properties of these four groups. Statistical comparisons were made between all groups, but only significant differences are shown, which correspond to p-values below 0.05.



Scheme 1. Iron oxide nanoparticles were synthesized via thermal decomposition of iron oleate precursor in an experimental setup that allowed eight (8) simultaneous reactions and post-synthesis oxidation treatments (PO). The effect of post-synthesis oxidation was studied by comparing two control groups that were not treated, C1 and C2, and two treated groups, PO3 and PO30.

Post-synthesis oxidation did not significantly affect nanoparticle size distribution and aspect ratio

Nanoparticle physical properties, such as size and shape, were investigated via bright field transmission electron microscopy (TEM), and representative images are shown in Figure 1a and Figure 1b, corresponding to sample PO3 5 (D_p = 18.5 nm) and PO3 3 (D_p = 29.2 nm). TEM images and histograms for all samples are included in the Supplementary Information (Figure S1-S4). We noted that the shape of the particles varied from spherical to slightly elongated, and therefore Figures 1a and 1b are representative of the samples with the lowest and the highest aspect ratio (AR), respectively. Because particles deviate from sphericity, the physical diameter calculated from their two-dimensional projections in TEM corresponds to that of a sphere with equivalent projected area. The distribution of the volume-weighted median physical diameter of the tracers is shown in Figure 1c for each of the four synthesis groups, with no statistically significant difference between groups and a global average of 23.5 nm. The distribution of the geometric deviation of the physical diameter, In σ_p , is shown in Figure 1d. A statistically significant difference was observed between C1 and the other three groups. However, values of $\ln \sigma_0$ were below 0.1 for all groups and are monodisperse. The AR is the ratio of the longest and the shortest lengths of the projected particle shape captured from TEM images, which ranged from 1.1 to 1.3. Figure 1a is a representative TEM image of nanoparticles with AR = 1.1, while Figure 1b is a representative TEM image of nanoparticles with AR = 1.3. The distribution of AR values was consistent across synthesis groups (Figure 1e); however, a linear relationship was found between AR and physical size for both C and PO groups, with a correlation coefficient (R2) of 0.55 and 0.93, respectively (Figure 1f). Shape anisotropy, here measured as the AR, has been observed to increase with nanoparticle size in thermal decomposition synthesis. 50 Although these irregularities can be often overlooked, Vanhecke et al. has demonstrated with electron microscopy and small angle x-ray scattering that the shape of nanoparticles synthesized by thermal decomposition can evolve from spherical to elongated as the reaction progresses, supporting the trend observed of increasing aspect ratio with increasing physical size. 65 These comparisons suggest that our synthesis setup resulted in nanoparticles with similar physical properties that were not affected by post-synthesis oxidation.

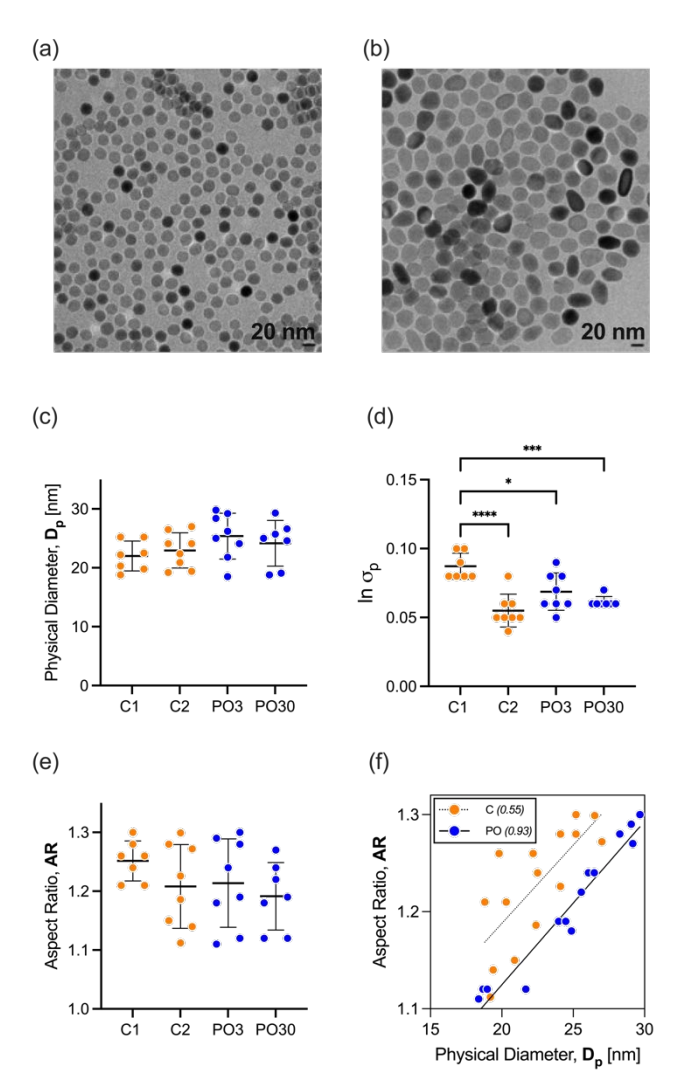


Figure 1. Tracer physical size and aspect ratio (AR) evaluated from transmission electron microscopy (TEM) are consistent across synthesis conditions. Representative TEM images of tracer with (a) the lowest physical size and AR (PO3_5, D_p = 18.5 nm, AR = 1.1), and (b) with the largest physical size and AR (PO3_3, D_p = 29.2 nm, AR = 1.3). Comparisons of (c) volume-weighted median physical diameter (D_p), (d) geometric deviation (In σ_p), and (e) AR, for the control and post-synthesis oxidation conditions suggest these properties are consistent across groups and not significantly affected by post-synthesis oxidation. In (d) the P-values obtained from the ordinary one-way ANOVA analysis comparison of C1 to C2, PO3, and PO30 were: p<0.0001 (****), p = 0.0123 (*), and p = 0.0006 (****), respectively. (f) AR as a function of the volume-weighted median physical diameter, with correlation coefficients in parenthesis in the legend (R^2).

Post synthesis oxidation resulted in increased magnetic diameters and saturation magnetization

SQUID magnetometry was used to evaluate the nanoparticle's magnetic properties, measuring the magnetization vs magnetic field (MH) curves to evaluate superparamagnetic behavior (Figure S5), and determine the magnetic diameter and saturation magnetization. For this, PEG-coated nanoparticles suspended in water were analyzed, as described under methods. The volume-weighted median magnetic diameter, determined from fitting of the MH curve to the Langevin function, significantly increases with post-synthesis oxidation from an average of 9 nm for control groups to 18 nm (Figure 2a) for post-synthesis oxidation groups, with statistically significant differences between the control and post-synthesis oxidation groups (p < 0.0001, *****). In contrast, there were no statistically significant differences in magnetic diameter between groups C1 and C2, and PO3 and PO30. Distributions of the geometric deviation of the magnetic diameter show no statistically significant differences (Figure 2b), except between groups C2 and PO3 (p = 0.0121). We noted that the geometric deviations for the magnetic diameter were consistently larger than 0.2, whereas the geometric deviations for the physical diameters (Figure 1d) were consistently smaller than 0.1. A paired t-test comparing ln σ_m and ln σ_p confirmed the difference is statistically significant (p < 0.0001, *****), supporting the notion that the underlying

magnetic diameters of the particles are more polydisperse than their physical diameters. Furthermore, it is evident from comparing Figure 1d and Figure 2b that the distribution of values for $\ln \sigma_m$ is broader than that for $\ln \sigma_p$, suggesting greater variation in magnetic properties relative to physical size. This difference can be more clearly observed in Figure S6.

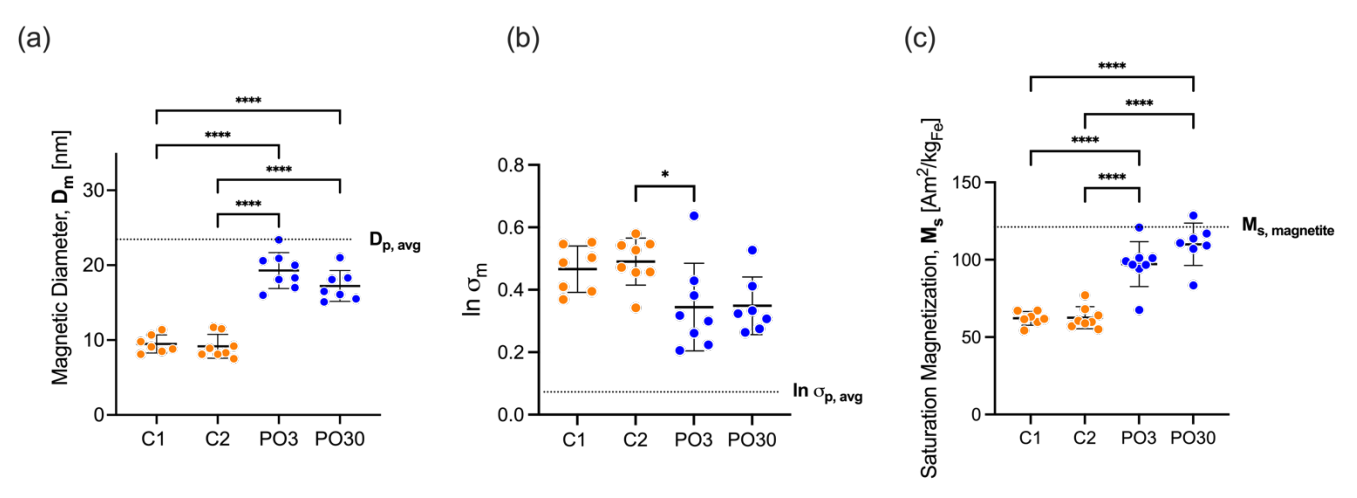


Figure 2. Tracer magnetic properties, magnetic diameter (D_m) and saturation magnetization (M_s), increase with post-synthesis oxidation. Comparisons of (a) volume-weighted median magnetic diameter (D_m), (b) geometric deviation ($In \sigma_m$), and (c) saturation magnetization (M_s) all suggest improvements in magnetic properties after post-synthesis oxidation treatment. The p-values obtained from the ordinary one-way ANOVA analysis were: (a) p<0.0001 (****), (b) p = 0.035 (*), and (c) p<0.0001 (****).

Post-synthesis oxidation resulted in nanoparticles with increased saturation magnetization compared to control, with some individual replicates having saturation magnetization close to that of bulk magnetite. Here we report properties such as saturation magnetization relative to iron mass, instead of magnetite, as the latter would require an assumption of the crystalline phase. The bulk saturation magnetization of magnetite is $86 \, \text{Am}^2/\text{kg}_{\text{Fe}3O4}$, and conversion to iron mass basis results in a saturation magnetization of $120 \, \text{Am}^2/\text{kg}_{\text{Fe}}$. The average saturation magnetization for the control and post-synthesis oxidation groups was $62.4 \, \text{and} \, 111.5 \, \text{Am}^2/\text{kg}_{\text{Fe}}$, respectively. Post-synthesis oxidation increased the saturation magnetization from 52% to 93% of the bulk value for magnetite (Figure 2c), with comparisons showing statistically significant differences between each control and post-synthesis oxidation group (p < 0.0001, ****) and no statistically significant differences when comparing C1 to C2 and PO3 to PO30. No strong correlation was observed when probing the dependence of the saturation magnetization on the physical diameter (D_p) (Figure S7). We note that although the magnetic diameter and saturation magnetization both increased with post-synthesis oxidation, there is still an inherent variability in these values. Furthermore, we note that two replicates (one in the PO3 group and one in the PO30 group) had saturation magnetization values slightly above the bulk value. We attribute this to inherent error in estimating iron mass.

Post-synthesis oxidation resulted in improved MPI resolution and signal intensity

MPI performance was characterized using MPI RELAXTM scans obtained in the MOMENTUMTM scanner, which uses a 16 mT 45 kHz excitation field and measures the magnetization for a field sweep between -160 mT and 160 mT. Point-spread functions (PSF) were obtained for each sample and normalized by iron mass to allow for comparison of different nanoparticles (Figure S8). The maximum signal intensity corresponds to sensitivity, while the full-width half-maximum (FWHM) corresponds to resolution. Comparison of individual control (C1 and C2) and post-synthesis oxidation (PO3 and PO30) groups did not result in statistically significant differences. Post-synthesis oxidation improved MPI performance by increasing signal intensity from an average of 14 mV/mg_{Fe} for the control groups to an average of 47 mV/mg_{Fe} for the post-synthesis oxidation groups (Figure 3a). Differences between control and post-synthesis oxidation groups were statistically significant with p-values of 0.0041 (**) for C1 vs PO30, 0.0022 (**) for C2 vs PO30, 0.0394 (*) for C1 vs PO3, and 0.0233 (*) for C2 vs PO3. Resolution also improved due to post-synthesis oxidation, with an average FWHM of 22 mT for the control groups and of 12 mT for the post-synthesis oxidation groups (Figure 3b). Again, differences between control and post-synthesis oxidation groups were statistically significant (p<0.0001, ****). Using similar methods in the same

MOMENTUM scanner we have previously reported that the commercial nanoparticle Ferucarbotran had FWHM of 11.2 mT and a signal intensity of 25.8 $\rm mg_{Fe}^{-1}$, whereas the commercial nanoparticle Synomag[®]-D had a FWHM of 9.2 mT and a signal intensity of 87.8 $\rm mg_{Fe}^{-1}$. ¹⁵

Beyond these inter-group comparisons, we noted that the spread of the signal intensity and FWHM also varied between control and post-synthesis oxidation groups. For signal intensity, the standard deviation was 7.2 mV/mgFe for the control groups and 23.8 mV/mgFe for the post-synthesis oxidation groups, taken together. This suggests that while post-synthesis oxidation resulted in increased signal intensity, it also resulted in greater variability in this MPI performance characteristic. On the contrary, for the FHWM the standard deviation was 3.6 mT for the control groups and 1.7 mT for the post-synthesis oxidation groups, suggesting that post-synthesis oxidation reduced variability in resolution. To effectively compare MPI signal intensity and FWHM, which are measurements with different units and are changing in opposite directions, the relative variability was calculated using the coefficient of variation (CV), the ratio of standard deviation to the mean. For signal intensity, the CV was 50% for both the control and post-synthesis oxidation groups, meanwhile for the FWHM the CV was 16% and 14% for the control and post-synthesis oxidation groups, respectively. This comparison suggests that the MPI signal intensity has a larger variation than the FWHM, independent from the post-synthesis oxidation treatment. Clearly, post-synthesis oxidation plays a role in producing nanoparticles with enhanced MPI performance, but further work is necessary to control variability in the resulting properties.

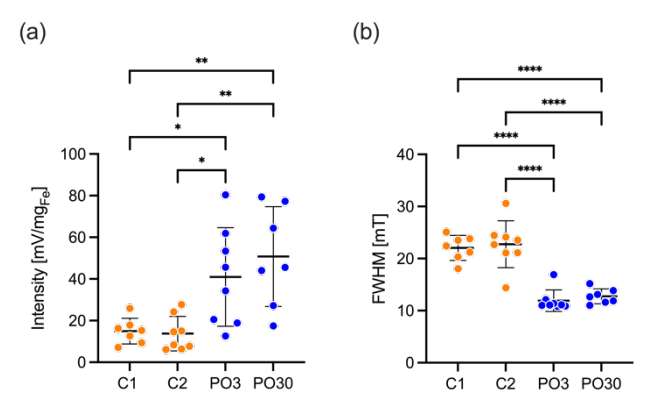


Figure 3. Post-synthesis oxidation improves MPI performance. Comparisons of PSF (a) peak specific intensity (mV/mg_{Fe}) and (b) full-width-half-maximum (FWHM, mT) suggest improvements in sensitivity and resolution due to post-synthesis oxidation. The P-values obtained from the ordinary one-way ANOVA analysis were: (a) from top to bottom p = 0.0041 (**), p = 0.0022 (**), p = 0.0394 (*), and p = 0.0233 (*), and in (b) p<0.0001 (****).

MPI performance correlations deviate from the predictions of the Langevin model

Here we explore how MPI performance correlates to values of physical and magnetic diameters and saturation magnetization, to test if these correlations conform to the predictions of the simple Langevin model, given by equations (1) and (2). Because we did not find statistically significant differences in mean physical diameter, aspect ratio, mean magnetic diameter, or saturation magnetization between C1 and C2 or between PO3 and PO30, below we distinguish solely between particles obtained without, denoted as C, and with, denoted as PO, post-synthesis oxidation.

First, we investigated correlations of MPI signal intensity and FWHM to physical diameter, the measure of nanoparticle size most often reported in the literature. According to the Langevin model, signal intensity should vary with the cube of the particle diameter and FWHM should vary with the inverse cube of the particle diameter. Figure 4a shows signal intensity plotted as a function of the cube of the physical diameter. Contrary to the predictions of equation (1), signal intensity decreases with increasing physical diameter cubed, for both the control and post-synthesis oxidation groups. Figure 4b shows FWHM plotted as a function of the inverse of the cube of the physical diameter. As with signal intensity, the FWHM data does not follow the predictions of the Langevin model, given by equation (2) in this case.

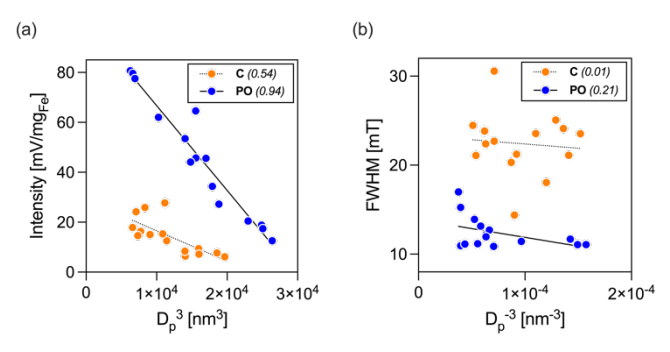


Figure 4. MPI performance correlations to tracer physical size deviate from Langevin model. Correlations to MPI (a) intensity and (b) FWHM are opposite to the expected improvement with the cube of the physical diameter for both control and post-synthesis oxidation groups. The correlation coefficients (R^2) are given in parenthesis in the legend.

Next, we investigated correlations of MPI signal intensity and FWHM to magnetic diameter. We note that results in Figures 1 and 2 show that there was greater variability in the nanoparticle's median magnetic diameter and geometric deviation. Figure 5a suggests that for the control groups, signal intensity is strongly correlated ($R^2 = 0.92$) with the cube of the magnetic diameter, as expected from equation (1) assuming the diameter in the equation is the magnetic diameter. On the contrary, for the post-synthesis oxidation groups the signal intensity is negatively correlated with the cube of the magnetic diameter, in contradiction with the predictions of equation (1). For resolution, Figure 5b shows that for the control groups FWHM is correlated with the inverse cube of the magnetic diameter, albeit with a relatively weak correlation coefficient ($R^2 = 0.44$). This agrees with equation (2). However, for the post-synthesis oxidation groups, Figure 5b shows a very weak correlation with inverse cube of the magnetic diameter, in disagreement with equation (2).

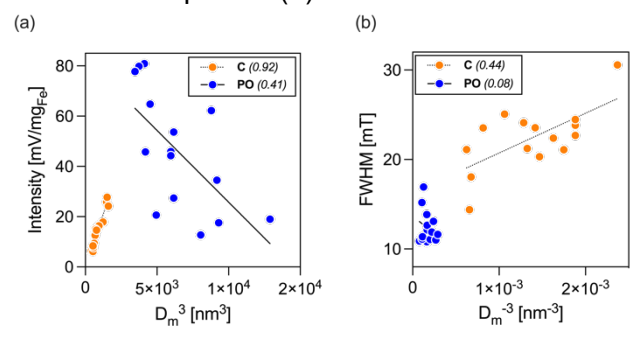


Figure 5. MPI performance correlations to tracer magnetic size show agreement with the Langevin model for the control group but deviate for the post-synthesis oxidation group. (a) MPI intensity strongly correlates to the cube of the magnetic diameter for the control group ($R^2 = 0.92$), meanwhile the post-synthesis oxidation group opposes Langevin expectations. (b) MPI FWHM weakly correlates to the inverse of the cube of the magnetic diameter for the control group ($R^2 = 0.44$), meanwhile the post-synthesis oxidation group does not. The correlation coefficients (R^2) are given in parenthesis in the legend.

Next, we noted that in addition to varying in physical and magnetic diameter, the control and post-synthesis oxidation groups had variability in their saturation magnetization (Figure 2c). We did not see strong correlations between MPI signal intensity or FWHM with saturation magnetization alone (Figure S9), however, we noted that saturation magnetization and cube of diameter appear together in equations (1) and (2). Figure 6 shows the signal intensity plotted as a function of the product of saturation magnetization and cube of magnetic diameter (Figure 6a) and FWHM plotted as a function of the inverse of the product of saturation magnetization and cube of the magnetic diameter (Figure 6b). A strong positive correlation is seen for the signal intensity and FWHM for the control groups (R² of 0.89 for signal intensity and 0.50 for FHWM), in agreement with equations (1) and (2). However, an inverse and weaker correlation is seen for the post-synthesis oxidation groups, in disagreement with the predictions of equations (1) and (2). Additionally, differences in the effective hydrodynamic diameter (Dh) were observed (Figure S10a) between the control and post-synthesis oxidation groups, however, no correlation to MPI performance (Figure S11), aspect ratio (Figure S12a), or magnetic diameter (Figure S12b) was found. Overall, these comparisons suggest that the simple Langevin model predictions of equations (1) and (2) are incapable of capturing the variability in MPI performance observed in the synthesized nanoparticles.

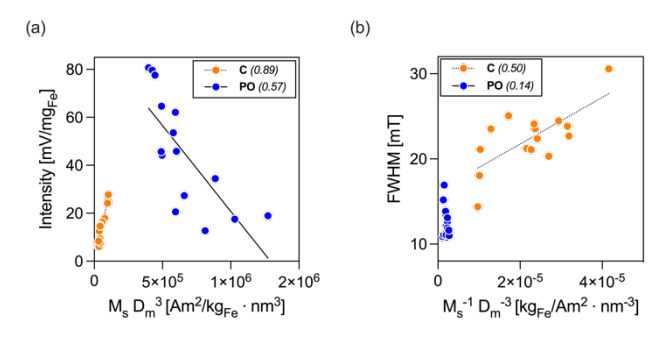


Figure 6. MPI performance correlations to the product of the saturation magnetization and the cubic magnetic diameter ($M_sD_m^3$) show agreement with the Langevin model for the control group but deviate for the post-synthesis oxidation group. (a) MPI intensity has a strong positive correlation to $M_sD_m^3$ for the control group ($R^2 = 0.89$), while the post-synthesis oxidation group shows a negative correlation. (b) MPI FWHM correlates positively to the inverse of $M_sD_m^3$ for the control group ($R^2 = 0.50$), and the post-synthesis oxidation group does not. The correlation coefficients (R^2) are given in parenthesis in the legend.

Shape anisotropy and discrepancy between physical and magnetic diameters negatively impact MPI performance

Next, we sought to determine if deviations from ideal superparamagnetic behavior, introduced by shape anisotropy and the discrepancy between physical and magnetic diameter, could explain trends in MPI performance of the nanoparticles. In fact, simulation studies suggest that MPI performance of anisotropic particles can be sensitive to the sampling trajectory used during image acquisition.⁶⁶ Others have previously studied the effects of size and shape on MPI performance. However, such studies were typically limited to small size ranges and lacked sufficient replicates for statistical testing, and presented contradictory results. For example, one study evaluated differences in harmonic spectra for particles with different polydisperse size distributions and structures, including single-core, multicore, and chainlike arrangements.⁶⁷ These authors suggest that particles that were large and had low effective anisotropy, arising from an unspecified combination of size and structure, had better MPI signal intensity and resolution. However, they studied a single sample representative of each condition and the four studied samples had a narrow range in shape. Another suggested that shape anisotropy of ~50 nm long and ~ 8 nm wide nanorods improves their MPI performance.⁶⁸ However, this study provided very limited physical and magnetic characterization of the nanoparticles used and the claim is based on comparison between ~50 nm long nanorods and ~13 nm spherical nanoparticles. It is well established that small spherical particles are poor MPI tracers. The study also lacked evaluation of multiple batches of nanoparticles to enable statistical analysis and evaluate reproducibility. As magnetic core size largely impacts MPI performance, we explore the effect of shape anisotropy in the narrower physical size range of this study for samples with smaller and larger magnetic core sizes, corresponding to the control and post-synthesis oxidation groups, respectively. First, shape anisotropy can be expected to result in an increase in particle relaxation time because of the introduction of an easy axis along the long dimension of the particle.31, 32, 69 It has been shown in the literature that relaxation degrades MPI performance and asymmetrically blurs the PSF in the scanning direction, which is analogous to an increase in center offset.³¹ Simulations of dynamic magnetization of idealized particles also suggests that center offset increases with increasing effects of finite magnetic relaxation.³¹ As a surrogate for direct measurements of particle anisotropy or of nanoparticle relaxation we used the shift in the peak of the PSF, called the center offset. Figure 7 plots the center offset as a function of aspect ratio for control and post-synthesis oxidation groups, showing the corresponding PSF peak intensity for each nanoparticle using a color scale. Center offset increases in the direction of the scan as AR increases for both control and post-synthesis oxidation groups, with an R² of 0.52 and 0.82, respectively. Furthermore, the color scale suggests that signal intensity decreases with increasing AR. However, we cannot isolate the effect of AR completely, as it correlates positively with particle size (Figure 1f), and both are expected to increase relaxation time. Comparing control and post-synthesis oxidation groups, the larger R² and slope for the post-synthesis oxidation group suggests a stronger effect of AR on the performance of the nanoparticles in this group, which could explain why the post-synthesis oxidation nanoparticles were observed to deviate from the predictions of equations (1) and (2) in the analysis above.

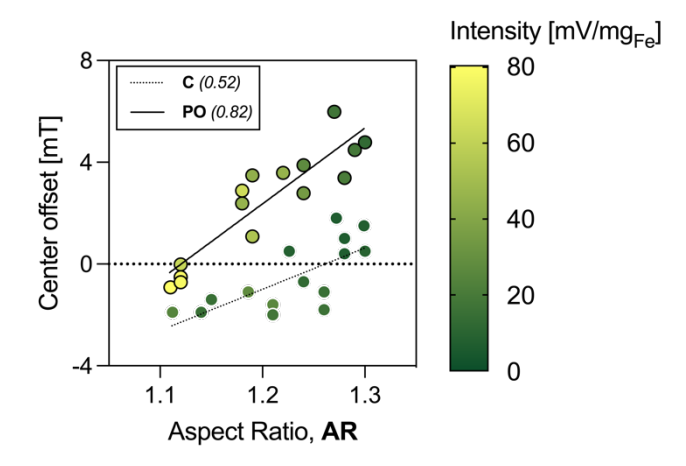


Figure 7. Shape anisotropy from increasing AR negatively impacts MPI performance by shifting the PSF peak, with a stronger effect on the post-synthesis oxidation group. The center offset is a measure of the shift of the PSF obtained directly from MPI RELAXTM measurements, and it shows positive correlations with AR for both control ($R^2 = 0.52$) and post-synthesis oxidation groups ($R^2 = 0.82$). The color scale shows MPI intensity, which was heavily impacted by increasing AR and center offset for the post-synthesis oxidation group.

Another factor that could introduce deviations from the ideal Langevin model is the discrepancy between physical and magnetic diameters of the particles. This discrepancy can be evidence of crystal defects, presence of multiple magnetic domains or phases within particles, or the existence of a so-called magnetically dead layer. As such, we sought to understand trends in this discrepancy for the control and post-synthesis oxidation groups. Figure 8 plots the magnetic diameter against the physical diameters for all nanoparticles in the control and post-synthesis oxidation groups, with AR values represented using a color scale. The dashed line corresponds to parity between the two diameters. Clearly, most particles have a significant discrepancy between physical and magnetic diameters. Interestingly, the discrepancy correlates differently with physical diameter for the control and post-synthesis oxidation groups. The discrepancy between physical and magnetic diameters increases more rapidly for the control group than for the post-synthesis oxidation group. Furthermore, it appears that nanoparticles with the smallest values of AR had the smallest discrepancy between physical and magnetic diameters.

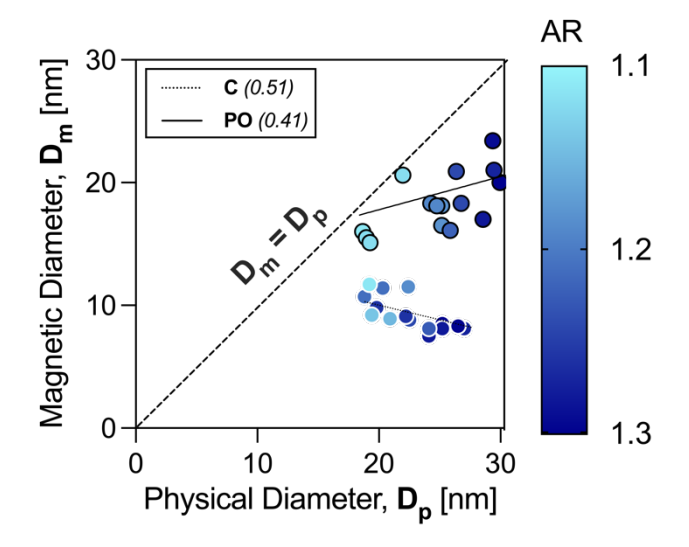


Figure 8. Post-synthesis oxidation partially reduces discrepancy between physical and magnetic diameters, D_p and D_m , respectively. The discrepancy between diameters increases with increasing D_p and AR for both groups, deviating from the ideal $D_m = D_p$ that is indicated by the dashed line. However, D_p correlates negatively with D_m for the control group, and it correlates positively for the post-synthesis oxidation group, highlighting the efficacy of the treatment. The correlation coefficients (R^2) are given in parenthesis in the legend.

Having established that shape anisotropy and discrepancies between magnetic and physical diameters are prevalent in both control and post-synthesis oxidation nanoparticles, next we sought to evaluate if these deviations from ideal particle properties can explain trends in MPI performance. Figure 9 is a plot of MPI resolution (FWHM) against signal intensity for all nanoparticles in the study, with shape anisotropy (AR) represented by the size of the markers and discrepancy between physical and magnetic diameter represented using a color scale. Particles in the lower right quadrant of the plot represent the best combination of resolution and signal intensity. Most of the nanoparticles from the control group are in the upper left quadrant, corresponding to poor MPI performance. The control nanoparticles also have the largest discrepancy between physical and magnetic diameters. Nanoparticles from the post-synthesis oxidation group are distributed in the bottom half of the figure, corresponding to better resolution, with several nanoparticles in the lower right quadrant, corresponding to the best MPI performance of the group. Importantly, the best performing nanoparticles also have among the lowest values of AR and smallest discrepancy between physical and magnetic diameters.

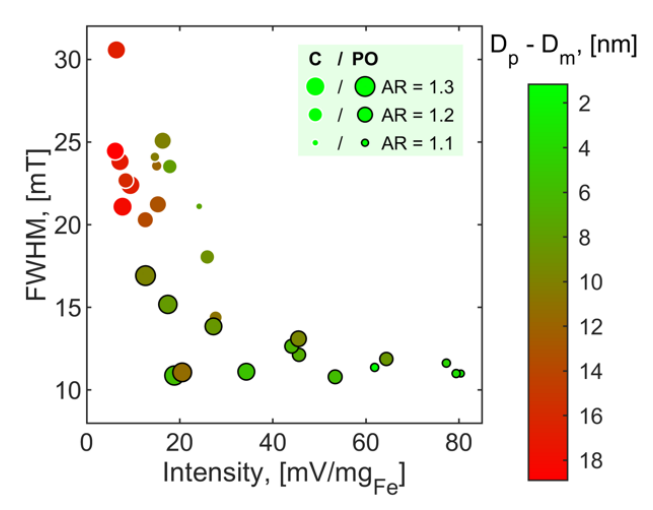


Figure 9. Tracers with the best MPI performance have low discrepancy between physical and magnetic diameters (D_p - D_m) and aspect ratio (AR). MPI FWHM and intensity are plotted to compare performance of control (markers with white borders) and post-synthesis oxidation nanoparticles (markers with black border). The size of the marker corresponds to AR and the color scale corresponds to D_p - D_m , suggesting that minimizing these improves MPI performance.

Pearson Correlations of MPI performance

As shown above, our results suggest that post-synthesis oxidation effectively increases D_m and M_s, decreasing D₀-Dm, and improving MPI performance. A Pearson correlation matrix was used to quantify the direction and magnitude of correlations between MPI performance, and tracer physical properties, magnetic properties, and center offsets measured in this study. Results for control and post-synthesis oxidation groups are shown in Figure 10, where the color scale represents the direction and magnitude of the correlation. As optimization of MPI performance corresponds to increasing intensity and reducing FWHM, improvement of performance translates to positive correlations for intensity and negative correlations for FWHM. MPI intensity of the control nanoparticles show the strongest correlations with D_m , $\ln \sigma_m$, and D_p - D_m , with values of 0.97, -0.82, -0.87, respectively. Interestingly, for the post-synthesis oxidation group the strongest correlations are with D_p, AR, and center-offset, with values of -0.96, -0.97, -0.91. This change in the strongest correlations from magnetic properties to physical properties suggests that shape anisotropy effects dominate for the post-synthesis oxidation group and hinder further improvement in MPI performance. For the FWHM, the strongest correlations for the control group are observed with D_m, M_s, and D_p-D_m, with values of -0.64, -0.43, 0.32, respectively. Stronger correlations were found for the post-synthesis oxidation group with $\ln \sigma_m$, center offset, and D_p , with values of 0.84, 0.64, and 0.53, respectively. However, correlations to AR and D_p-D_m are almost similarly as strong with values of 0.51 and 0.50. As with MPI intensity, the properties that correlate the strongest to FWHM change from being dominated by magnetic properties for the control group to physical properties for the post-synthesis oxidation group. Increasing tracer size, either physical or magnetic via post-synthesis oxidation, poses the challenge of increased relaxation effects that deviate performance from that expected from the Langevin model.

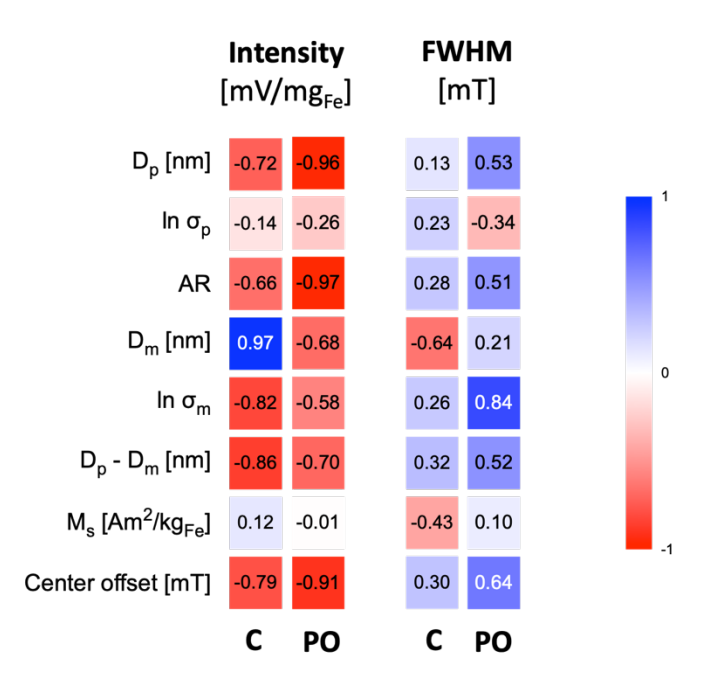


Figure 10. Correlations to MPI performance are dominated by magnetic properties for the control (C) group and by physical properties for the post-synthesis oxidation (PO) group. The Pearson correlation matrix relates MPI intensity and FWHM to tracer properties and the scan center offset for control and post-synthesis oxidation groups. The color scale represents the direction and magnitude of the correlation, where positive correlations are desired to improve MPI intensity (increase), and negative correlations are desired to improve the FWHM (decrease).

Discussion

The results of this study demonstrate the significant effect of post-synthesis oxidation on the magnetic properties and MPI performance of iron oxide nanoparticles synthesized via thermal decomposition of iron oleate for use as MPI tracers. The findings reveal that post-synthesis oxidation leads to an increase in magnetic diameter and saturation magnetization, improving MPI performance in terms of signal intensity and resolution. However, a large variation in performance is observed for the post-synthesis oxidation groups (Figure 3), which we partly attribute to the larger variation in magnetic diameter, geometric distribution, and saturation magnetization compared to the control groups. Correlations to the tracer size often reported, the physical diameter, show disagreement from the predictions of the Langevin model, equations (1) and (2), for both control and post-synthesis oxidation groups (Figure 4). Correlations to magnetic diameter and its product with the saturation magnetization show agreement with the Langevin model for the control group and disagreement for the post-synthesis oxidation group (Figure 6). Aiming to understand the root of these deviations, correlations with other properties were probed. The study highlights the negative impact on MPI performance of shape anisotropy by relating the aspect ratio to the shift of the PSF obtained from MPI RELAXTM scans, the center-offset, which has been previously attributed to relaxation effects and degradation of MPI signal. Results show that increasing aspect ratio, and hence increasing shape anisotropy, correlates with increasing center offset, which we attribute to increasing relaxation effects for both the control and post-synthesis oxidation groups (Figure 7). Since the effect is greater for the post-synthesis oxidation group, results suggest that shape anisotropy and relaxation effects are most likely responsible for the disagreement from the Langevin model, which assumes negligible relaxation and uniform magnetization.

Post-synthesis oxidation reduces the discrepancy between physical and magnetic diameters (D_p - D_m), however, its effectiveness is limited as tracer size increases for the conditions explored in this study. Nanoparticles with the best MPI performance have low aspect ratio and small discrepancy between physical and magnetic diameters, highlighting the need to carefully control these properties in the design and synthesis of MPI tracers. The Pearson correlation matrix identified the magnetic properties that correlate strongest to MPI performance for the control group, while also revealing a change in the strongest correlations from magnetic properties for the control group to physical properties for the post-synthesis oxidation group. These results

provide valuable insight into the challenges introduced by increasing relaxation and shape control when synthesizing tracers tailored for MPI. Still, we believe that post-synthesis oxidation shows tremendous potential as a processing step in the synthesis of tracers with superior MPI performance.

Conclusions

This study elucidates the impact of post-synthesis oxidation on both the magnetic properties and MPI performance of iron oxide nanoparticles synthesized via thermal decomposition of iron oleate. The post-synthesis oxidation treatment enhances saturation magnetization and magnetic diameter, effectively enhancing MPI signal intensity and resolution. Nonetheless, we observe discrepancies between actual MPI performance and predictions based on the Langevin model. These deviations are most likely attributable to shape anisotropy and relaxation effects, which are more pronounced in the post-synthesis oxidation group. Furthermore, the study highlights the limited effectiveness of post-synthesis oxidation in reducing the gap between physical and magnetic diameters as tracer size increases. Optimal MPI tracers obtained in this study are characterized by a low aspect ratio and minimal discrepancy between physical and magnetic diameters. Analysis of Pearson's correlations reveals a shift in the strongest correlations from magnetic to physical properties following post-synthesis oxidation, suggesting new challenges in tracer synthesis due to increased relaxation and shape control. Despite these challenges, post-synthesis oxidation emerges as a promising avenue for enhancing the MPI performance of tracers, underscoring the need for fine control of both physical and magnetic properties in their design and synthesis.

Materials and Methods

Materials

Iron (III) acetylacetonate (>98% pure) and 3-aminopropyltrimethoxysilane (APS, >98%) were purchased from TCI American (Portland, OR). Oleic acid (90% technical grade) was purchased from Alfa Aesar (Haverhill, MA). 1-octadecene (90%), polyethylene glycol monomethyl ether (mPEG, 5kDa), sulfuric acid (99.999%), and isopropyl alcohol (70%) were purchased from Sigma-Aldrich (St. Louis, MO). Toluene (>99.5%, ACS reagent), ethanol (200 proof), acetone (certified ACS), chromium trioxide (crystalline, certified ACS), diethyl ether (certified ACS), hydrochloric acid (37% w/v), 1-ethyl-3-(3-dimethylaminopropyl) carbodiimide (EDC), activated charcoal (12-40 mesh), diethyl ether (ACS chemical, BHT stabilized), dichloromethane (99.6%, ACS reagent), nitric acid (Certified ACS Plus), potassium hydroxide (85%, ACS reagent), and CBQCA protein quantitation kit were purchased from Thermo Fisher Scientific (Waltham, MA). N-hydroxysulfo- succinimide (sulfo-NHS) was purchased from ProteoChemTM (Hurricane, UT). Copper TEM grid (carbon film only, 200 mesh) was purchased from TED PELLA, INC (Redding, CA).

Particle Synthesis

Synthesis of iron (III) oleate

Iron oleate was prepared according to published work with some modifications. ¹⁵ Iron acetylacetonate (22.38 g, 63.36 mmol) was combined with oleic acid (89.48 g, 316.80 mmol) in a 1:5 molar ratio inside a 500 mL 3-neck round bottom flask. The flask was then introduced into a molten metal bath set at 110°C, with a condenser, thermocouple, and overhead stirrer in the 3 necks. The condenser was connected to a chiller set to 12°C and attached to the right neck of the reactor. The overhead stirring, set up in the middle neck, was set to a rate of 350 rpm. The thermocouple and gas flow needle were held by a septum in the left neck, with the argon gas flow set to 100 sccm. Once the equipment was set up, the molten metal bath was ramped up in temperature to a setpoint of 325°C at a rate of 6.2 °C/min. After the reaction crosses 300°C, close monitoring requires taking aliquots with a syringe and SS needle through the septum in the left neck. FTIR is used to scan aliquots in real-time and determine the reaction endpoint, controlling the percentage of free oleic acid left in the oleate. Once the free oleic acid present in the precursor mixture was estimated to be close to 35%, the reactor was taken off heating, and the mixture was recovered, purged with Argon, and stored for use in iron oxide nanoparticle synthesis in the following two days.

Synthesis of magnetic iron oxide nanoparticles

Iron oxide nanoparticles were synthesized using a high throughput approach, running eight reactions simultaneously in 15 mL PYREXTM glass tubes using a molten metal bath as the heating element. Reaction conditions were chosen based on published work 50 and scaled down to a reaction volume of 5 mL. The following reagents were pipetted into each pyrex tube: 3207 μL (11.3 mmol) of 1-octadecene, 968 μL (3.05 mmol) of oleic acid, and 825 μL (0.5 mmol) of iron oleate synthesized as described above. Custom 3D printed septum-like caps made of flexible resin were used and the reaction vials were agitated using a vortex to homogenize the reaction mixture. Finally, reaction vials were placed in a custom 3D printed holder made of high temperature resin, submerged halfway into the molten metal bath, and attached to a gas manifold supplying 50 sccm of Argon to each reaction vial using a mass flow controller. The molten metal bath was heated to 340°C at a rate of 5°C/min, to reach an internal reaction temperature of 330°C. Once the reaction temperature was reached, the reaction was maintained for two hours and ten minutes. To finalize the reaction, the reactor holder and manifold was lifted out of the molten metal bath and allowed to cool before capping with a septum for storage. Toluene and ethanol were used in a 2:3 volume ratio to precipitate nanoparticles from the crude synthesis product, and the pellet was resuspended with toluene via sonication, resulting in oleic acid coated particles.

Post-synthesis oxidation

Control samples (C1 and C2) were stored directly after synthesis, meanwhile post-synthesis oxidation samples were re-introduced to the molten metal bath at a lower temperature of 300°C. A mixture of 1% Oxygen in Argon was supplied at a rate of 50 sccm to each vial using the same gas manifold for a total time of either 3 of 30 hours for samples labeled PO3 and PO30, respectively.

Particle coating

PEG-silane synthesis

A poly(ethylene glycol)-silane (PEGSilane) conjugate was formed via a two-step procedure. First, methyl ether poly(ethylene glycol) (mPEG) was oxidized to bear a carboxylic acid on its terminal end opposite the methyl end via a Jones Oxidation method. Jones Reagent was made by preparing 70 g of Chromium Trioxide in 500 mL of deionized water and 61mL of sulfuric acid. Then, 40 g of mPEG was dissolved in 500 mL Acetone and 16.1 mL of Jones reagent was added to the mixture while stirring and allowed to react for 24 hours. Following the oxidation reaction, 5 mL of isopropanol was added to the solution to quench the reaction and 5 g of activated charcoal was added to adsorb the chromium salts. These salts and charcoal were then removed via vacuum filtration. The acetone solution was reduced via rotary evaporation to concentrate the solution, then added to a separatory funnel with 50 mL of 1M hydrochloric acid (HCI). The polymer was then extracted via liquid-liquid separation, by adding diethyl ether to the solution, agitating, letting settle, then extracting the aqueous phase. Then, this aqueous phase was added back to the separatory funnel, followed by addition of dichloromethane. The separatory funnel was agitated, let to settle, and the organic phase was collected. This organic phase was concentrated via rotary evaporation and precipitated via diethyl ether addition. This polymer extract was then dried in a vacuum oven at room temperature for 24 hours. In the second step, mPEG-COOH was converted to PEGSilane via an amidation reaction with 3-aminopropyltrimethoxysilane (APTES). Briefly, 20 g of mPEG-COOH was added to a round bottom flask and placed into an oil bath at 120°C. Then, APTES was added to the melted PEG in a 1:1 molar ratio, and the mixture was stirred and allowed to react at 120°C and 500 mbar. Following the reaction, the PEGSilane was cooled to room temperature and collected.

High-temperature ligand exchange

Tracers were coated with a PEGSilane shell via a ligand exchange procedure, replacing the oleic acid surface with PEGSilane, following procedures described previously. First, PEGSilane was dissolved in dry toluene using a dry heating block at 101°C. Then, oleic acid coated tracers in toluene were ultrasonicated and added to the PEGSilane solution followed by 3-aminopropyltrimethoxysilane (APTES), vortexed, capped, then allowed to react at 101°C in the dry heating block overnight. The resulting solution, containing PEGSilane coated tracers, was precipitated via diethyl ether addition and subsequent centrifugation. The supernatant was discarded, and the precipitate was dried in a vacuum oven at room temperature overnight. The resulting pellet consisting of PEGSilane coated tracers and excess polymer was suspended in deionized water via vortexing and sonication.

Transmission Electron Microscopy

$$n_N(D_p) = \frac{1}{\sqrt{2\pi}D_p \ln \sigma_p} \exp\left(-\frac{\ln^2 D_p/D_{pgv}}{2\ln^2 \sigma_g}\right)$$
 (3)

 D_{pq} was converted to a volume median diameter (D_{pgv}) using:

$$D_{pgv} = \exp\left[lnD_{pg} + 3ln^2\sigma_p\right] \tag{4}$$

Dynamic Light Scattering

The hydrodynamic size of the PEG-coated nanoparticles in deionized water was determined using a DynaPro plate reader for dynamic light scattering measurements at room temperature. The effective hydrodynamic diameter (D_h) is compared for all groups in the Supplementary Information (Figures S10a), meanwhile the polydispersity index (PDI) is compared for samples that did not exhibit a multimodal population (Figure S10b).

Magnetometry and magnetic diameter fitting

Magnetic characterization was conducted using a magnetic property measurement system (MPMS-3) superconducting quantum interference device (SQUID) magnetometer (Quantum Design, Inc. CA, USA). PTFE sample holders were loaded with 100 μ L of PEGSilane coated tracers suspended in deionized water at concentrations ranging from 0.1 to 1 mg Fe/mL. Magnetization versus magnetic field (MH) curves were acquired at 300K to confirm superparamagnetic behavior (Figure S5) and fit the data to the Langevin function $L(\alpha)$ for superparamagnetism (equations 5 and 6), weighted using a lognormal size distribution ($n_V(D_m)$) (equation 7), as suggested by Chantrell *et al.* ⁷²

$$M(\alpha) = M_S \int_0^\infty n_v(D_m) L(\alpha) dD_m ,$$

$$L(\alpha) = \coth \alpha - \frac{1}{\alpha}; \ \alpha = \frac{\pi \mu_0 M_d D_m^3 H}{6k_B T},$$
(6)

(6)
$$n_{v}(D_{m}) = \frac{1}{\sqrt{2\pi}D_{m}\ln\sigma_{m}} \exp\left[-\frac{\ln^{2}(D_{m}/D_{mv})}{2\ln^{2}\sigma}\right]$$
 (7)

where α is the Langevin parameter, M_s is the saturation magnetization of the sample, D_{mv} is the volume-weighted median magnetic diameter, $In \sigma_m$ is the geometric deviation of the magnetic diameter distribution, μ_0 is the permeability of free space, k_B is Boltzmann's constant, M_d is the domain magnetization of the magnetic nanoparticles, and T is the absolute temperature. The magnetization curves were fitted to these equations using a nonlinear regression model in MATLAB, providing an estimate of the average magnetic diameters, under the assumption that the magnetic domains are spherical. The saturation magnetization was obtained from the maximum of the magnetization curves, normalized by mass of iron.

MPI performance characterization

MPI performance of nanoparticle samples was characterized by acquiring MPI RELAXTM scans using the MOMENTUMTM scanner (Magnetic Insight, CA, USA). The PEG-Si coated tracers suspended in DI water were loaded into 0.2 mL microcentrifuge tubes at concentrations ranging from 0.1 to 1 mg Fe/ mL and volumes ranging from 10-200 μ L. Each sample was placed in custom 3D printed sample holder ¹⁵, centered in the MPI FOV, and scanned for 3-5min. The signal of the x-space point spread function (PSF) obtained using the RELAXTM scan modality was normalized by iron mass to facilitate comparisons. The MPI signal corresponds to the peak specific intensity reported in units of mV/mg_{Fe}, and the resolution corresponds to the FWHM reported as the system reported value in units of mT.

Statistical Analysis

GraphPad Prism software was used to perform ordinary one-way ANOVA statistical analysis to compare the means of properties across the four different synthesis groups: C1, C2, PO3, and PO30 in Figures 1-3. The P-

value tests the hypothesis that samples from all groups are from populations with identical means, allowing us to statistically test the effect of the post-synthesis oxidation treatment. If the P values are large, the data suggests that the means do not differ and there is no statistically significant difference. On the other hand, if the P values are below 0.05, there is statistically significant difference between groups. Correlation coefficients (R^2) were obtained from simple linear regressions. The Pearson correlation matrix obtained using the Prism software uses two-tailed P values to quantify the direction and magnitude of correlations. This analysis was performed to screen for correlations between MPI performance and all the nanoparticle properties measured in this study.

Acknowledgements

Research reported in this publication was supported by the National Institute for Biomedical Imaging and Bioengineering of the National Institutes of Health under award number R01EB031224, by the National Cancer Institute under award number R21CA263653, the National Institute of Neurological Disorders and Stroke under award number R21NS125089, and the National Science Foundation Research Experiences for Undergraduates Program under award number EEC-1852111. The content is solely the responsibility of the authors and does not necessarily represent the official views of the National Institutes of Health or the National Science Foundation.

Supporting Information: Derivation of equation (1); representative TEM, magnetization curve, and MPI performance results for all samples; additional statistical analyses and correlation plots; tabulated physical and magnetic properties and MPI performance for all samples.

References

- (1) Gleich, B.; Weizenecker, J. Tomographic imaging using the nonlinear response of magnetic particles. *Nature* **2005**, 435 (7046), 1214-1217. DOI: 10.1038/nature03808 (acccessed 2022/01/10/19:01:40). From www.nature.com.
- (2) Lu, Y.; Rivera-Rodriguez, A.; Tay, Z. W.; Hensley, D.; Fung, K. L. B.; Colson, C.; Saayujya, C.; Huynh, Q.; Kabuli, L.; Fellows, B.; et al. Combining magnetic particle imaging and magnetic fluid hyperthermia for localized and image-guided treatment. *International Journal of Hyperthermia* **2020**, *37* (3), 141-154. DOI: 10.1080/02656736.2020.1853252 (acccessed 2022/01/10/16:23:43). From Taylor and Francis+NEJM.
- (3) Orendorff, R.; Peck, A. J.; Zheng, B.; Shirazi, S. N.; Ferguson, R. M.; Khandhar, A. P.; Kemp, S. J.; Goodwill, P.; Krishnan, K. M.; Brooks, G. A.; et al. Firstin vivotraumatic brain injury imaging via magnetic particle imaging. *Physics in Medicine and Biology* **2017**, *62* (9), 3501-3509. DOI: 10.1088/1361-6560/aa52ad (acccessed 2022/01/10/16:11:27). From Institute of Physics.
- (4) Nejadnik, H.; Pandit, P.; Lenkov, O.; Lahiji, A. P.; Yerneni, K.; Daldrup-Link, H. E. Ferumoxytol Can Be Used for Quantitative Magnetic Particle Imaging of Transplanted Stem Cells. *Mol Imaging Biol* **2019**, *21* (3), 465-472. DOI: 10.1007/s11307-018-1276-x (acccessed 2022/01/10/16:14:56). From Springer Link.
- (5) Rivera-Rodriguez, A.; Hoang-Minh, L. B.; Chiu-Lam, A.; Sarna, N.; Marrero-Morales, L.; Mitchell, D. A.; Rinaldi-Ramos, C. M. Tracking adoptive T cell immunotherapy using magnetic particle imaging. *Nanotheranostics* **2021**, *5* (4), 431-444. DOI: 10.7150/ntno.55165 (acccessed 2022/01/10/16:26:51). From PubMed Central.
- (6) Zheng, B.; Vazin, T.; Goodwill, P. W.; Conway, A.; Verma, A.; Ulku Saritas, E.; Schaffer, D.; Conolly, S. M. Magnetic Particle Imaging tracks the long-term fate of in vivo neural cell implants with high image contrast. *Sci Rep* **2015**, *5* (1), 14055. DOI: 10.1038/srep14055 (acccessed 2023-02-01T00:33:46).
- (7) Zheng, B.; Von See, M. P.; Yu, E.; Gunel, B.; Lu, K.; Vazin, T.; Schaffer, D. V.; Goodwill, P. W.; Conolly, S. M. Quantitative Magnetic Particle Imaging Monitors the Transplantation, Biodistribution, and Clearance of Stem Cells <i>In Vivo</i>In Vivo
- (8) Savliwala, S.; Chiu-Lam, A.; Unni, M.; Rivera-Rodriguez, A.; Fuller, E.; Sen, K.; Threadcraft, M.; Rinaldi, C. Magnetic nanoparticles. In *Nanoparticles for Biomedical Applications*, Elsevier, 2020; pp 195-221.
- (9) Chandrasekharan, P.; Tay, Z. W.; Zhou, X. Y.; Yu, E.; Orendorff, R.; Hensley, D.; Huynh, Q.; Fung, K. L. B.; VanHook, C. C.; Goodwill, P.; et al. A perspective on a rapid and radiation-free tracer imaging modality, magnetic particle imaging, with promise for clinical translation. *BJR* **2018**, *91* (1091), 20180326. DOI: 10.1259/bjr.20180326 (acccessed 2022/01/13/16:42:46). From birpublications.org (Atypon).
- (10) Arami, H.; Teeman, E.; Troksa, A.; Bradshaw, H.; Saatchi, K.; Tomitaka, A.; Gambhir, S. S.; Häfeli, U. O.; Liggitt, D.; Krishnan, K. M. Tomographic magnetic particle imaging of cancer targeted nanoparticles. *Nanoscale* **2017**, *9* (47), 18723-18730. DOI: 10.1039/c7nr05502a From PubMed.

- (11) Prévot, G.; Kauss, T.; Lorenzato, C.; Gaubert, A.; Larivière, M.; Baillet, J.; Laroche-Traineau, J.; Jacobin-Valat, M. J.; Adumeau, L.; Mornet, S.; et al. Iron oxide core oil-in-water nanoemulsion as tracer for atherosclerosis MPI and MRI imaging. *International Journal of Pharmaceutics* **2017**, *532* (2), 669-676. DOI: https://doi.org/10.1016/j.ijpharm.2017.09.010.
- (12) Tay, Z. W.; Chandrasekharan, P.; Chiu-Lam, A.; Hensley, D. W.; Dhavalikar, R.; Zhou, X. Y.; Yu, E. Y.; Goodwill, P. W.; Zheng, B.; Rinaldi, C.; et al. Magnetic Particle Imaging-Guided Heating in Vivo Using Gradient Fields for Arbitrary Localization of Magnetic Hyperthermia Therapy. *ACS Nano* **2018**, *12* (4), 3699-3713. DOI: 10.1021/acsnano.8b00893 (acccessed 2022/01/09/23:58:23). From ACS Publications.
- (13) Meola, A.; Rao, J.; Chaudhary, N.; Song, G.; Zheng, X.; Chang, S. D. Magnetic Particle Imaging in Neurosurgery. *World Neurosurgery* **2019**, *125*, 261-270. DOI: 10.1016/j.wneu.2019.01.180 (acccessed 2021/06/28/21:56:03). From ScienceDirect.
- (14) Antonelli, A.; Szwargulski, P.; Scarpa, E.-S.; Thieben, F.; Cordula, G.; Ambrosi, G.; Guidi, L.; Ludewig, P.; Knopp, T.; Magnani, M. Development of long circulating magnetic particle imaging tracers: use of novel magnetic nanoparticles and entrapment into human erythrocytes. *Nanomedicine* **2020**, *15* (8), 739-753. DOI: 10.2217/nnm-2019-0449 (acccessed 2023/01/31).
- (15) Liu, S.; Chiu-Lam, A.; Rivera-Rodriguez, A.; DeGroff, R.; Savliwala, S.; Sarna, N.; Rinaldi-Ramos, C. M. Long circulating tracer tailored for magnetic particle imaging. *Nanotheranostics* **2021**, *5* (3), 348-361. DOI: 10.7150/ntno.58548 (acccessed 2022/01/10/17:11:27). From PubMed Central.
- (16) Song, G.; Chen, M.; Zhang, Y.; Cui, L.; Qu, H.; Zheng, X.; Wintermark, M.; Liu, Z.; Rao, J. Janus Iron Oxides @ Semiconducting Polymer Nanoparticle Tracer for Cell Tracking by Magnetic Particle Imaging. *Nano Lett.* **2018**, *18* (1), 182-189. DOI: 10.1021/acs.nanolett.7b03829 (acccessed 2023-02-01T01:28:41).
- (17) Wang, Q.; Ma, X.; Liao, H.; Liang, Z.; Li, F.; Tian, J.; Ling, D. Artificially Engineered Cubic Iron Oxide Nanoparticle as a High-Performance Magnetic Particle Imaging Tracer for Stem Cell Tracking. *ACS Nano* **2020**, *14* (2), 2053-2062. DOI: 10.1021/acsnano.9b08660 (acccessed 2023-02-01T00:52:14).
- (18) Sehl, O. C.; Foster, P. J. The sensitivity of magnetic particle imaging and fluorine-19 magnetic resonance imaging for cell tracking. *Sci Rep* **2021**, *11* (1), 22198. DOI: 10.1038/s41598-021-01642-3 (acccessed 2022/02/03/22:06:08). From www.nature.com.
- (19) Khandhar, A. P.; Keselman, P.; Kemp, S. J.; Ferguson, R. M.; Goodwill, P. W.; Conolly, S. M.; Krishnan, K. M. Evaluation of PEG-coated iron oxide nanoparticles as blood pool tracers for preclinical magnetic particle imaging. *Nanoscale* **2017**, *9* (3), 1299-1306. DOI: 10.1039/c6nr08468k (acccessed 2023-02-01T00:40:08).
- (20) Kratz, H.; Mohtashamdolatshahi, A.; Eberbeck, D.; Kosch, O.; Wiekhorst, F.; Taupitz, M.; Hamm, B.; Stolzenburg, N.; Schnorr, J. Tailored Magnetic Multicore Nanoparticles for Use as Blood Pool MPI Tracers. *Nanomaterials* **2021**, *11* (6), 1532. DOI: 10.3390/nano11061532 (acccessed 2023-02-15T19:49:01).
- (21) Kratz, H.; Taupitz, M.; Ariza De Schellenberger, A.; Kosch, O.; Eberbeck, D.; Wagner, S.; Trahms, L.; Hamm, B.; Schnorr, J. Novel magnetic multicore nanoparticles designed for MPI and other biomedical applications: From synthesis to first in vivo studies. *PLOS ONE* **2018**, *13* (1), e0190214. DOI: 10.1371/journal.pone.0190214 (acccessed 2023-02-01T00:57:50).
- (22) Rahmer, J.; Antonelli, A.; Sfara, C.; Tiemann, B.; Gleich, B.; Magnani, M.; Weizenecker, J.; Borgert, J. Nanoparticle encapsulation in red blood cells enables blood-pool magnetic particle imaging hours after injection. *Physics in Medicine and Biology* **2013**, *58* (12), 3965-3977. DOI: 10.1088/0031-9155/58/12/3965 (acccessed 2023-02-01T01:37:31).
- (23) Goodwill, P. W.; Saritas, E. U.; Croft, L. R.; Kim, T. N.; Krishnan, K. M.; Schaffer, D. V.; Conolly, S. M. X-Space MPI: Magnetic Nanoparticles for Safe Medical Imaging. *Advanced Materials* **2012**, *24* (28), 3870-3877. DOI: 10.1002/adma.201200221 (acccessed 2022/04/05/15:03:10). From Wiley Online Library.
- (24) Goodwill, P. W.; Conolly, S. M. The X-Space Formulation of the Magnetic Particle Imaging Process: 1-D Signal, Resolution, Bandwidth, SNR, SAR, and Magnetostimulation. *IEEE Transactions on Medical Imaging* **2010**, *29* (11), 1851-1859. DOI: 10.1109/TMI.2010.2052284 From IEEE Xplore.
- (25) Biederer, S.; Knopp, T.; Sattel, T.; Ludtke-Buzug, K.; Gleich, B.; Weizenecker, J.; Borgert, J.; Buzug, T. Magnetization response spectroscopy of superparamagnetic nanoparticles for magnetic particle imaging. *Journal of Physics D-Applied Physics* **2009**, *42* (20), Article. DOI: 10.1088/0022-3727/42/20/205007.
- (26) Graeser, M.; Thieben, F.; Szwargulski, P.; Werner, F.; Gdaniec, N.; Boberg, M.; Griese, F.; Möddel, M.; Ludewig, P.; van de Ven, D.; et al. Human-sized magnetic particle imaging for brain applications. *Nat Commun* **2019**, *10* (1), 1936. DOI: 10.1038/s41467-019-09704-x (acccessed 2022/01/10/19:03:02). From www.nature.com.

- (27) Ferguson, R. M.; Khandhar, A. P.; Kemp, S. J.; Arami, H.; Saritas, E. U.; Croft, L. R.; Konkle, J.; Goodwill, P. W.; Halkola, A.; Rahmer, J.; et al. Magnetic Particle Imaging With Tailored Iron Oxide Nanoparticle Tracers. *IEEE Transactions on Medical Imaging* **2015**, *34* (5), 1077-1084. DOI: 10.1109/tmi.2014.2375065 (acccessed 2023-02-01T01:47:09).
- (28) Tay, Z. W.; Savliwala, S.; Hensley, D. W.; Fung, K. L. B.; Colson, C.; Fellows, B. D.; Zhou, X.; Huynh, Q.; Lu, Y.; Zheng, B.; et al. Superferromagnetic Nanoparticles Enable Order-of-Magnitude Resolution & Sensitivity Gain in Magnetic Particle Imaging. *Small Methods* **2021**, *5* (11), 2100796. DOI: 10.1002/smtd.202100796 (acccessed 2022/01/11/02:26:18). From Wiley Online Library.
- (29) Julia J. Gevaert, K. V. B., Olivia C. Sehl, Paula J. Foster. VivoTrax+ improves the detection of cancer cells with magnetic particle imaging. *International Journal on Magnetic Particle Imaging IJMPI* **2022**, *Vol* 8. (acccessed 2023-08-17T15:27:51).
- (30) Eberbeck, D.; Wiekhorst, F.; Wagner, S.; Trahms, L. How the size distribution of magnetic nanoparticles determines their magnetic particle imaging performance. *Appl. Phys. Lett.* **2011**, *98* (18), 182502. DOI: 10.1063/1.3586776 (acccessed 2022/01/11/21:23:27). From aip.scitation.org (Atypon).
- (31) Croft, L. R.; Goodwill, P. W.; Conolly, S. M. Relaxation in x-space magnetic particle imaging. *IEEE Trans Med Imaging* **2012**, *31* (12), 2335-2342. DOI: 10.1109/tmi.2012.2217979 From NLM.
- (32) Zhao, Z.; Garraud, N.; Arnold, D. P.; Rinaldi, C. Effects of particle diameter and magnetocrystalline anisotropy on magnetic relaxation and magnetic particle imaging performance of magnetic nanoparticles. *Phys. Med. Biol.* **2020**, *65* (2), 025014. DOI: 10.1088/1361-6560/ab5b83 (acccessed 2022/01/11/02:27:09). From Institute of Physics.
- (33) Bauer, L. M.; Situ, S. F.; Griswold, M. A.; Samia, A. C. S. Magnetic Particle Imaging Tracers: State-of-the-Art and Future Directions. *J. Phys. Chem. Lett.* **2015**, *6* (13), 2509-2517. DOI: 10.1021/acs.jpclett.5b00610 (acccessed 2021/06/28/20:32:08). From ACS Publications.
- (34) Hufschmid, R.; Arami, H.; Ferguson, R. M.; Gonzales, M.; Teeman, E.; Brush, L. N.; Browning, N. D.; Krishnan, K. M. Synthesis of phase-pure and monodisperse iron oxide nanoparticles by thermal decomposition. *Nanoscale* **2015**, *7* (25), 11142-11154. DOI: 10.1039/C5NR01651G (acccessed 2022/01/16/16:19:35). From pubs.rsc.org.
- (35) Tay, Z. W.; Hensley, D. W.; Vreeland, E. C.; Zheng, B.; Conolly, S. M. The Relaxation Wall: Experimental Limits to Improving MPI Spatial Resolution by Increasing Nanoparticle Core size. *Biomed. Phys. Eng. Express* **2017**, *3* (3), 035003. DOI: 10.1088/2057-1976/aa6ab6 (acccessed 2022/04/05/19:35:37). From PubMed Central.
- (36) Zhao, Z.; Rinaldi, C. Computational predictions of enhanced magnetic particle imaging performance by magnetic nanoparticle chains. *Phys. Med. Biol.* **2020**, *65* (18), 185013. DOI: 10.1088/1361-6560/ab95dd (acccessed 2022/01/11/02:26:56). From Institute of Physics.
- (37) Tay, Z.; Goodwill, P.; Hensley, D.; Taylor, L.; Zheng, B.; Conolly, S. A High-Throughput, Arbitrary-Waveform, MPI Spectrometer and Relaxometer for Comprehensive Magnetic Particle Optimization and Characterization. *Sci Rep* **2016**, *6*, Article. DOI: 10.1038/srep34180.
- (38) Kratz, H.; Mohtashamdolatshahi, A.; Eberbeck, D.; Kosch, O.; Hauptmann, R.; Wiekhorst, F.; Taupitz, M.; Hamm, B.; Schnorr, J. MPI Phantom Study with A High-Performing Multicore Tracer Made by Coprecipitation. *Nanomaterials* **2019**, *9* (10), 1466. DOI: 10.3390/nano9101466 (acccessed 2023-02-01T01:52:38).
- (39) Irfan, M.; Dogan, N.; Bingolbali, A.; Aliew, F. Synthesis and characterization of NiFe2O4 magnetic nanoparticles with different coating materials for magnetic particle imaging (MPI). *Journal of Magnetism and Magnetic Materials* **2021**, 537, 168150. DOI: https://doi.org/10.1016/j.jmmm.2021.168150.
- (40) Arami, H.; Ferguson, R. M.; Khandhar, A. P.; Krishnan, K. M. Size-dependent ferrohydrodynamic relaxometry of magnetic particle imaging tracers in different environments. *Medical Physics* **2013**, *40* (7), 071904. DOI: 10.1118/1.4810962 (acccessed 2022/01/11/21:46:07). From Wiley Online Library.
- (41) Goodwill, P.; Tamrazian, A.; Croft, L.; Lu, C.; Johnson, E.; Pidaparthi, R.; Ferguson, R.; Khandhar, A.; Krishnan, K.; Conolly, S. Ferrohydrodynamic relaxometry for magnetic particle imaging. *Appl. Phys. Lett.* **2011**, *98* (26), Article. DOI: 10.1063/1.3604009.
- (42) Dogan, N.; Dogan, O. M.; Irfan, M.; Ozel, F.; Kamzin, A. S.; Semenov, V. G.; Buryanenko, I. V. Manganese dopediron oxide nanoparticles and their potential as tracer agents for magnetic particle imaging (MPI). *Journal of Magnetism and Magnetic Materials* **2022**, *561*, 169654. DOI: https://doi.org/10.1016/j.jmmm.2022.169654.
- (43) Bauer, L. M.; Situ, S. F.; Griswold, M. A.; Samia, A. C. S. High-performance iron oxide nanoparticles for magnetic particle imaging guided hyperthermia (hMPI). *Nanoscale* **2016**, *8* (24), 12162-12169. DOI: 10.1039/c6nr01877g (acccessed 2023-02-01T01:42:12).

- (44) Dogan, N.; Caliskan, G.; Irfan, M. Synthesis and characterization of biocompatible ZnFe2O4 nanoparticles for magnetic particle imaging (MPI). *Journal of Materials Science: Materials in Electronics* **2023**, *34* (5). DOI: 10.1007/s10854-022-09799-x (acccessed 2023-02-15T23:40:40).
- (45) Silvestri, N.; Gavilán, H.; Guardia, P.; Brescia, R.; Fernandes, S.; Samia, A. C. S.; Teran, F. J.; Pellegrino, T. Di- and tricomponent spinel ferrite nanocubes: synthesis and their comparative characterization for theranostic applications. *Nanoscale* **2021**, *13* (32), 13665-13680. DOI: 10.1039/d1nr01044a (accessed 2023-02-01T00:02:04).
- (46) Morales, M. P.; Veintemillas-Verdaguer, S.; Montero, M. I.; Serna, C. J.; Roig, A.; Casas, L.; Martínez, B.; Sandiumenge, F. Surface and Internal Spin Canting in γ-Fe₂O₃ Nanoparticles. *Chem. Mater.* **1999**, *11* (11), 3058-3064. DOI: 10.1021/cm991018f (acccessed 2023-08-17T18:54:31).
- (47) Luigjes, B.; Woudenberg, S. M. C.; De Groot, R.; Meeldijk, J. D.; Torres Galvis, H. M.; De Jong, K. P.; Philipse, A. P.; Erné, B. H. Diverging Geometric and Magnetic Size Distributions of Iron Oxide Nanocrystals. *J. Phys. Chem. C* **2011**, *115* (30), 14598-14605. DOI: 10.1021/jp203373f (acccessed 2023-08-17T18:55:33).
- (48) Liebermann, L.; Clinton, J.; Edwards, D. M.; Mathon, J. "Dead" Layers in Ferromagnetic Transition Metals. *Physical Review Letters* **1970**, *25* (4), 232-235. DOI: 10.1103/physrevlett.25.232 (acccessed 2023-08-17T18:56:31).
- (49) Baaziz, W.; Pichon, B. P.; Fleutot, S.; Liu, Y.; Lefevre, C.; Greneche, J.-M.; Toumi, M.; Mhiri, T.; Begin-Colin, S. Magnetic Iron Oxide Nanoparticles: Reproducible Tuning of the Size and Nanosized-Dependent Composition, Defects, and Spin Canting. *J. Phys. Chem. C* **2014**, *118* (7), 3795-3810. DOI: 10.1021/jp411481p (acccessed 2023-08-17T18:57:35).
- (50) Kemp, S. J.; Ferguson, R. M.; Khandhar, A. P.; Krishnan, K. M. Monodisperse magnetite nanoparticles with nearly ideal saturation magnetization. *RSC Adv.* **2016**, *6* (81), 77452-77464. DOI: 10.1039/C6RA12072E (acccessed 2022/01/13/19:11). From pubs.rsc.org.
- (51) Unni, M.; Uhl, A. M.; Savliwala, S.; Savitzky, B. H.; Dhavalikar, R.; Garraud, N.; Arnold, D. P.; Kourkoutis, L. F.; Andrew, J. S.; Rinaldi, C. Thermal Decomposition Synthesis of Iron Oxide Nanoparticles with Diminished Magnetic Dead Layer by Controlled Addition of Oxygen. *ACS Nano* **2017**, *11* (2), 2284-2303. DOI: 10.1021/acsnano.7b00609 (acccessed 2022/01/13/15:33:48). From ACS Publications.
- (52) Chen, R.; Christiansen, M. G.; Sourakov, A.; Mohr, A.; Matsumoto, Y.; Okada, S.; Jasanoff, A.; Anikeeva, P. High-Performance Ferrite Nanoparticles through Nonaqueous Redox Phase Tuning. *Nano Lett.* **2016**, *16* (2), 1345-1351. DOI: 10.1021/acs.nanolett.5b04761 (acccessed 2022/01/16/19:13:53). From ACS Publications.
- (53) Du, Y.; Liu, X.; Liang, Q.; Liang, X.-J.; Tian, J. Optimization and Design of Magnetic Ferrite Nanoparticles with Uniform Tumor Distribution for Highly Sensitive MRI/MPI Performance and Improved Magnetic Hyperthermia Therapy. *Nano Lett.* **2019**, *19* (6), 3618-3626. DOI: 10.1021/acs.nanolett.9b00630 (acccessed 2022/01/09/23:26:07). From ACS Publications.
- (54) Ludwig, F.; Wawrzik, T.; Yoshida, T.; Gehrke, N.; Briel, A.; Eberbeck, D.; Schilling, M. Optimization of Magnetic Nanoparticles for Magnetic Particle Imaging. *IEEE Transactions on Magnetics* **2012**, *48* (11), 3780-3783. DOI: 10.1109/TMAG.2012.2197601 From IEEE Xplore.
- (55) Shasha, C.; Teeman, E.; Krishnan, K. M. Nanoparticle core size optimization for magnetic particle imaging. *Biomed. Phys. Eng. Express* **2019**, *5* (5), 055010. DOI: 10.1088/2057-1976/ab3972 (acccessed 2022/01/16/22:10:56). From DOI.org (Crossref).
- (56) Tomitaka, A.; Ota, S.; Nishimoto, K.; Arami, H.; Takemura, Y.; Nair, M. Dynamic magnetic characterization and magnetic particle imaging enhancement of magnetic-gold core—shell nanoparticles. *Nanoscale* **2019**, *11* (13), 6489-6496. DOI: 10.1039/c9nr00242a (acccessed 2023-02-01T01:45:52).
- (57) Avugadda, S. K.; Wickramasinghe, S.; Niculaes, D.; Ju, M.; Lak, A.; Silvestri, N.; Nitti, S.; Roy, I.; Samia, A. C. S.; Pellegrino, T. Uncovering the Magnetic Particle Imaging and Magnetic Resonance Imaging Features of Iron Oxide Nanocube Clusters. *Nanomaterials* **2020**, *11* (1), 62. DOI: 10.3390/nano11010062 (acccessed 2023-02-01T01:28:01).
- (58) Dadfar, S. M.; Camozzi, D.; Darguzyte, M.; Roemhild, K.; Varvarà, P.; Metselaar, J.; Banala, S.; Straub, M.; Güvener, N.; Engelmann, U.; et al. Size-isolation of superparamagnetic iron oxide nanoparticles improves MRI, MPI and hyperthermia performance. *Journal of Nanobiotechnology* **2020**, *18* (1). DOI: 10.1186/s12951-020-0580-1 (acccessed 2023-02-15T19:34:28).
- (59) Gloag, L.; Mehdipour, M.; Ulanova, M.; Mariandry, K.; Nichol, M. A.; Hernández-Castillo, D. J.; Gaudet, J.; Qiao, R.; Zhang, J.; Nelson, M.; et al. Zero valent iron core—iron oxide shell nanoparticles as small magnetic particle imaging tracers. *Chemical Communications* **2020**, *56* (24), 3504-3507. DOI: 10.1039/c9cc08972a (acccessed 2023-02-01T01:44:38).
- (60) Song, G.; Kenney, M.; Chen, Y.-S.; Zheng, X.; Deng, Y.; Chen, Z.; Wang, S. X.; Gambhir, S. S.; Dai, H.; Rao, J. Carbon-coated FeCo nanoparticles as sensitive magnetic-particle-imaging tracers with photothermal and magnetothermal

- properties. *Nature Biomedical Engineering* **2020**, *4* (3), 325-334. DOI: 10.1038/s41551-019-0506-0 (acccessed 2023-02-01T01:43:56).
- (61) Baki, A.; Remmo, A.; Löwa, N.; Wiekhorst, F.; Bleul, R. Albumin-Coated Single-Core Iron Oxide Nanoparticles for Enhanced Molecular Magnetic Imaging (MRI/MPI). *International Journal of Molecular Sciences* **2021**, *22* (12), 6235. DOI: 10.3390/ijms22126235 (accessed 2023-02-15T18:46:31).
- (62) Jiang, Z.; Han, X.; Du, Y.; Li, Y.; Li, Y.; Li, J.; Tian, J.; Wu, A. Mixed Metal Metal—Organic Frameworks Derived Carbon Supporting ZnFe₂0₄/C for High-Performance Magnetic Particle Imaging. *Nano Lett.* **2021**, *21* (7), 2730-2737. DOI: 10.1021/acs.nanolett.0c04455 (acccessed 2023-02-01T01:42:52).
- (63) Tay, Z. W.; Savliwala, S.; Hensley, D. W.; Fung, K. L. B.; Colson, C.; Fellows, B. D.; Zhou, X.; Huynh, Q.; Lu, Y.; Zheng, B.; et al. Superferromagnetic Nanoparticles Enable Order-of-Magnitude Resolution & Sensitivity Gain in Magnetic Particle Imaging. *Small Methods* **2021**, *5* (11), 2100796. DOI: 10.1002/smtd.202100796 (acccessed 2023-02-01T01:01:51).
- (64) Zhu, X.; Li, J.; Peng, P.; Hosseini Nassab, N.; Smith, B. R. Quantitative Drug Release Monitoring in Tumors of Living Subjects by Magnetic Particle Imaging Nanocomposite. *Nano Lett.* **2019**, *19* (10), 6725-6733. DOI: 10.1021/acs.nanolett.9b01202 (acccessed 2023-02-01T01:25:54).
- (65) Vanhecke, D.; Crippa, F.; Lattuada, M.; Balog, S.; Rothen-Rutishauser, B.; Petri-Fink, A. Characterization of the Shape Anisotropy of Superparamagnetic Iron Oxide Nanoparticles during Thermal Decomposition. *Materials* **2020**, *13* (9), 2018. DOI: 10.3390/ma13092018 (acccessed 2023-10-24T20:58:45).
- (66) Graeser, M.; Bente, K.; Neumann, A.; Buzug, T. M. Trajectory dependent particle response for anisotropic mono domain particles in magnetic particle imaging. *Journal of Physics D: Applied Physics* **2016**, *49* (4), 045007. DOI: 10.1088/0022-3727/49/4/045007.
- (67) Ota, S.; Matsugi, Y.; Nakamura, T.; Takeda, R.; Takemura, Y.; Kato, I.; Nohara, S.; Sasayama, T.; Yoshida, T.; Enpuku, K. Effects of size and anisotropy of magnetic nanoparticles associated with dynamics of easy axis for magnetic particle imaging. *Journal of Magnetism and Magnetic Materials* **2019**, *474*, 311-318. DOI: 10.1016/j.jmmm.2018.11.043 (acccessed 2023-10-18T19:07:12).
- (68) Nigam, S.; Mohapatra, J.; Makela, A. V.; Hayat, H.; Rodriguez, J. M.; Sun, A.; Kenyon, E.; Redman, N. A.; Spence, D.; Jabin, G.; et al. Shape Anisotropy-Governed High-Performance Nanomagnetosol for In Vivo Magnetic Particle Imaging of Lungs. *Small* **2023**. DOI: 10.1002/smll.202305300 (acccessed 2023-10-18T19:24:52).
- (69) Jurgen Weizenecker, B. G., Jurgen Rahmer and Jorn Borge. Micro-magnetic simulation study on the magnetic particle imaging performance of anisotropic mono-domain particles. *Phys. Med. Biol.* **2012**, *57*, 7317-7327. (acccessed 2023-03-15T18:01:14).
- (70) Zhu, M.-Q.; Chang, E.; Sun, J.; Drezek, R. A. Surface modification and functionalization of semiconductor quantum dots through reactive coating of silanes in toluene. *J. Mater. Chem.* **2007**, *17* (8), 800-805. DOI: 10.1039/b614432b (acccessed 2023-08-17T19:26:04).
- (71) Schindelin, J.; Arganda-Carreras, I.; Frise, E.; Kaynig, V.; Longair, M.; Pietzsch, T.; Preibisch, S.; Rueden, C.; Saalfeld, S.; Schmid, B.; et al. Fiji: an open-source platform for biological-image analysis. *Nature Methods* **2012**, *9* (7), 676-682. DOI: 10.1038/nmeth.2019 (acccessed 2023-08-17T19:27:44).
- (72) Chantrell, R.; Popplewell, J.; Charles, S. Measurements of particle size distribution parameters in ferrofluids. *IEEE Transactions on Magnetics* **1978**, *14* (5), 975-977. DOI: 10.1109/TMAG.1978.1059918 From IEEE Xplore.

Post-synthesis Oxidation of Superparamagnetic Iron Oxide Nanoparticles to Enhance Magnetic Particle Imaging (MPI) Performance

Ambar C. Velazquez-Albino¹, Aniela Nozka², Andrii Melnyk¹, Hayden J. Good¹, Carlos M. Rinaldi-Ramos^{1,3,+}

- 1. Department of Chemical Engineering, University of Florida, Gainesville, FL 32611
- 2. Department of Bioengineering, Clemson University, Clemson, SC 29634
- 3. J. Crayton Pruitt Family Department of Biomedical Engineering, University of Florida, Gainesville, FL 32611-6131

I. Supporting Results

Derivation of Equation 1:

In ref [24], Figure 4 shows the Langevin function, and how the point spread function (PSF) is the derivative of the Langevin function $(\dot{\mathcal{L}})$:

$$\dot{\mathcal{L}}[kH] = Nm\left(\frac{1}{(kH)^2} - \frac{1}{\sinh^2(kH)}\right)$$

The MPI sensitivity corresponds to the peak of the PSF, for which we can get an expression by calculating the limit at kH = 0.

$$\lim_{kH\to 0} Nm\left(\frac{1}{(kH)^2} - \frac{1}{\sinh^2(kH)}\right) = \frac{Nm}{3}$$

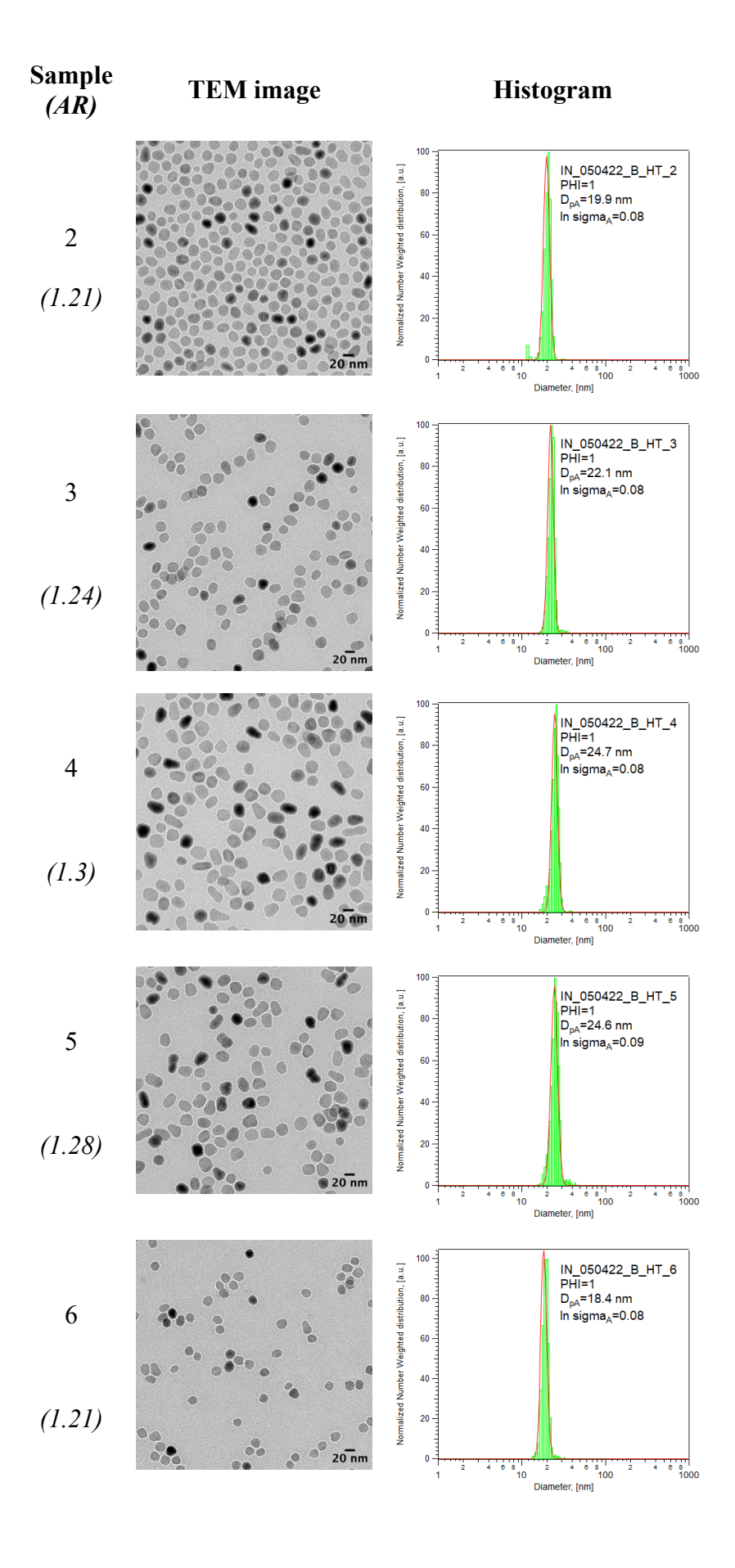
By substituting the equation for the magnetic moment (m)

$$m = \frac{\pi}{6} M_s D^3$$

We obtain that MPI signal from the peak intensity corresponds to Equation (1):

$$I = \frac{N\pi M_s D^3}{18}$$

⁺Corresponding author



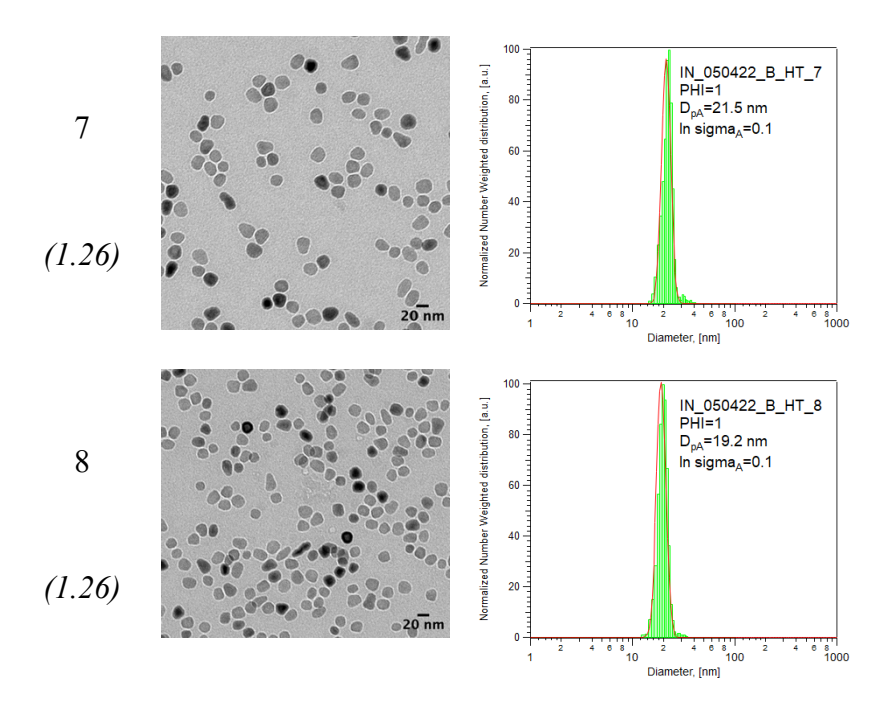
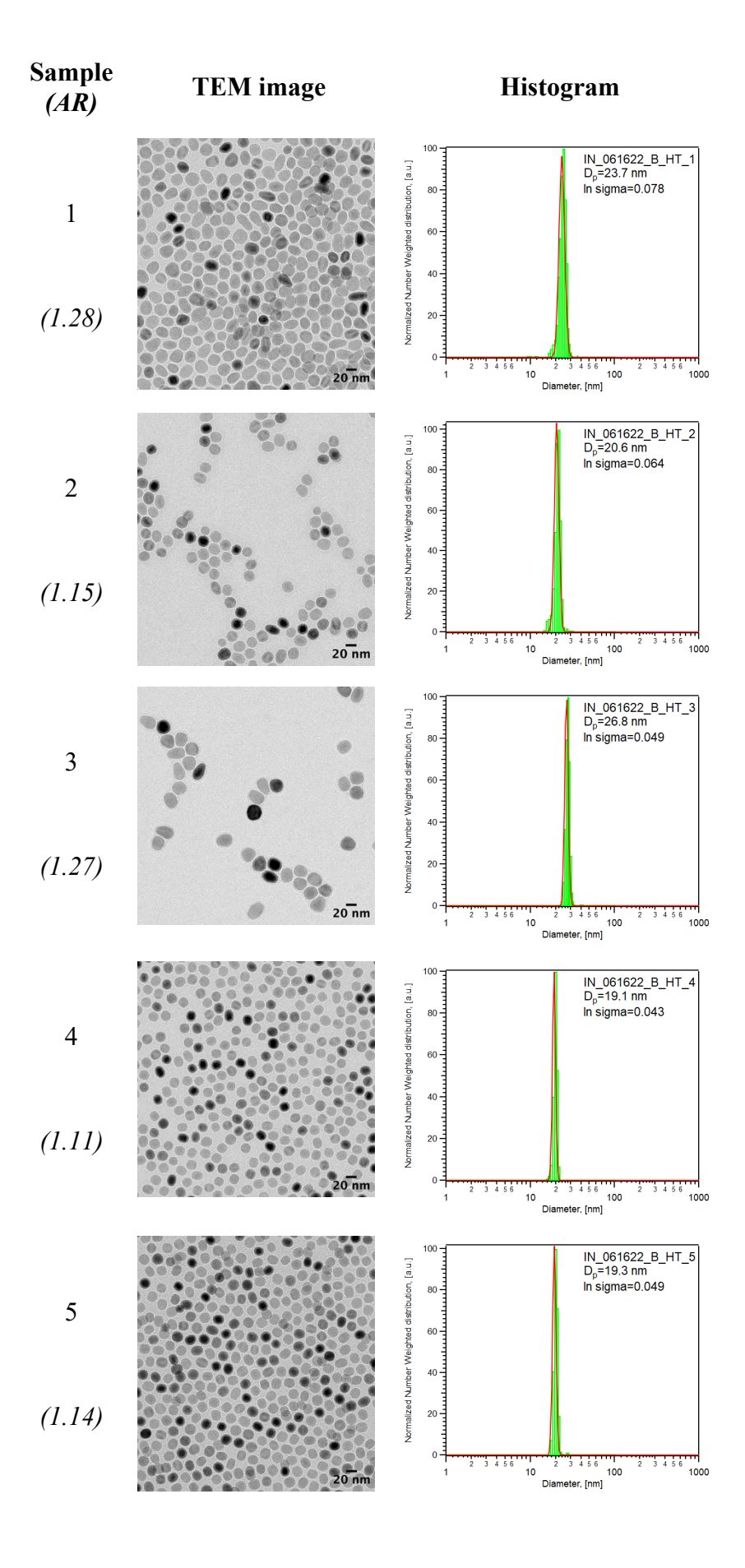


Figure S1. Representative TEM images and corresponding physical diameter distributions for all particles synthesized without any post-synthesis treatment in the control group 1 (C1).



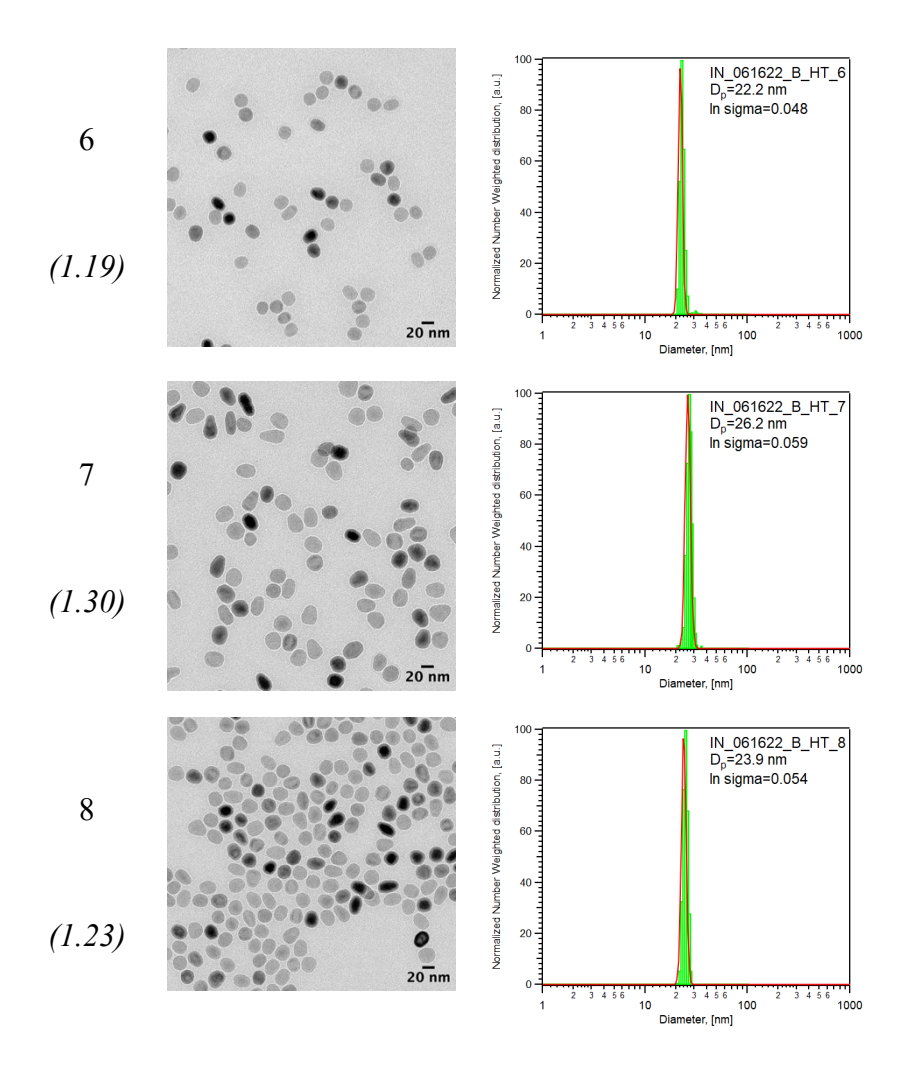
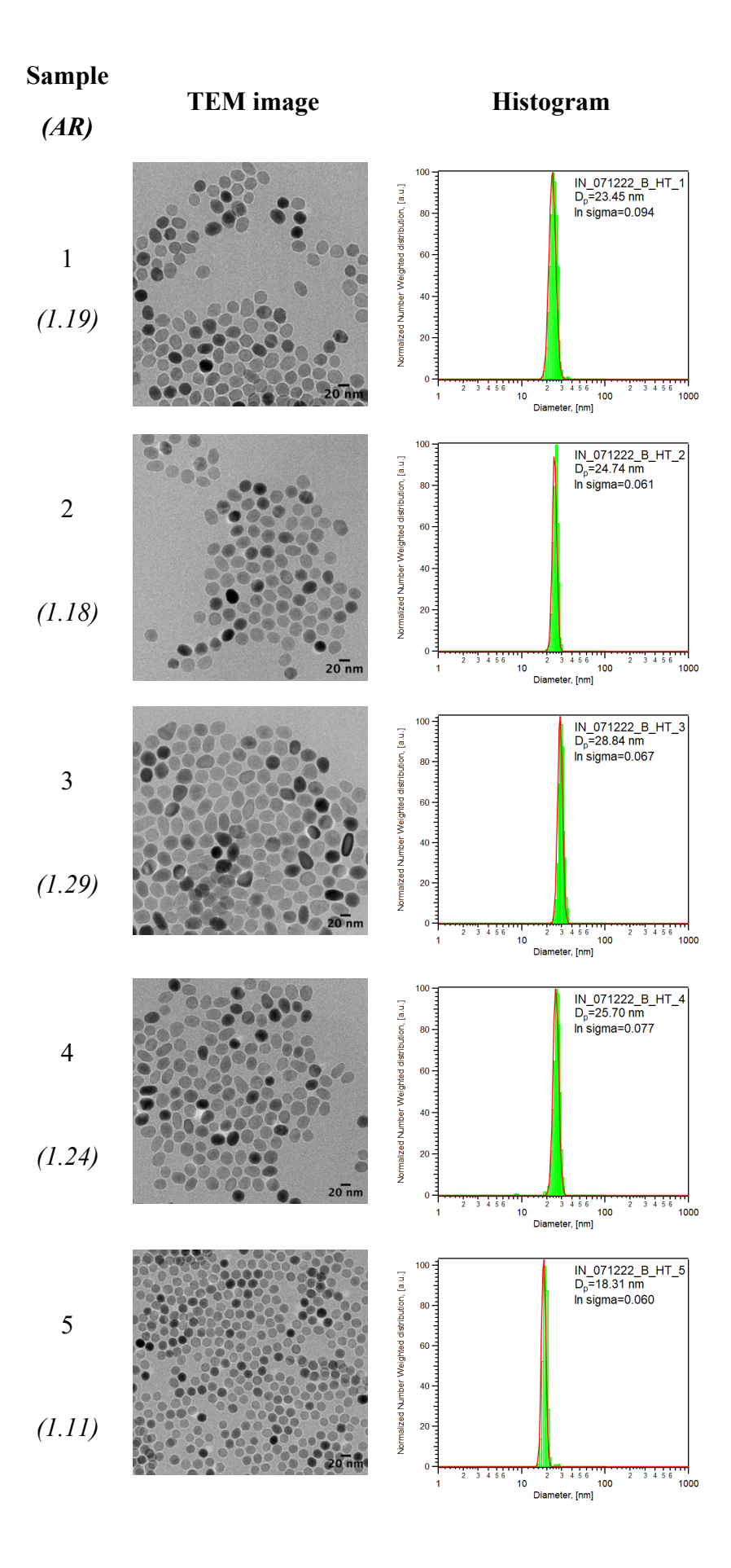


Figure S2. Representative TEM images and corresponding physical diameter distributions for all particles synthesized without any post-synthesis treatment in the control group 2 (C2).



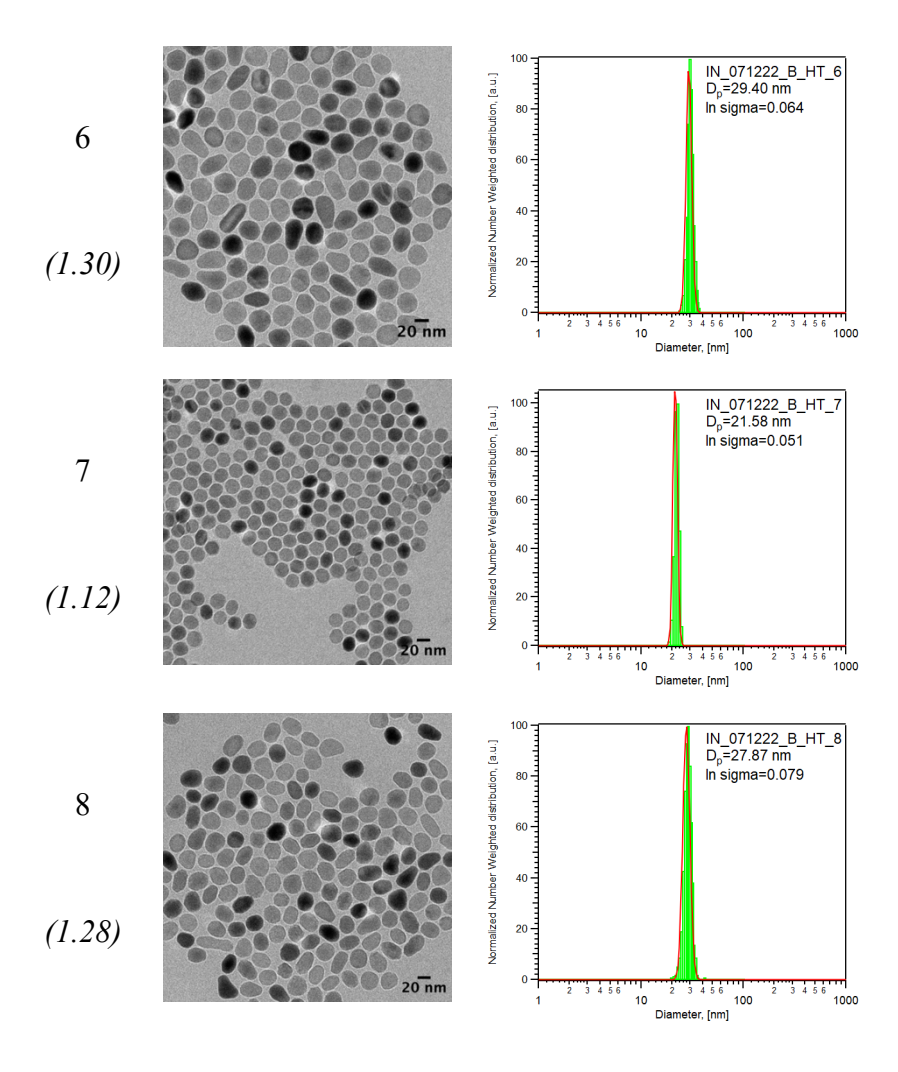
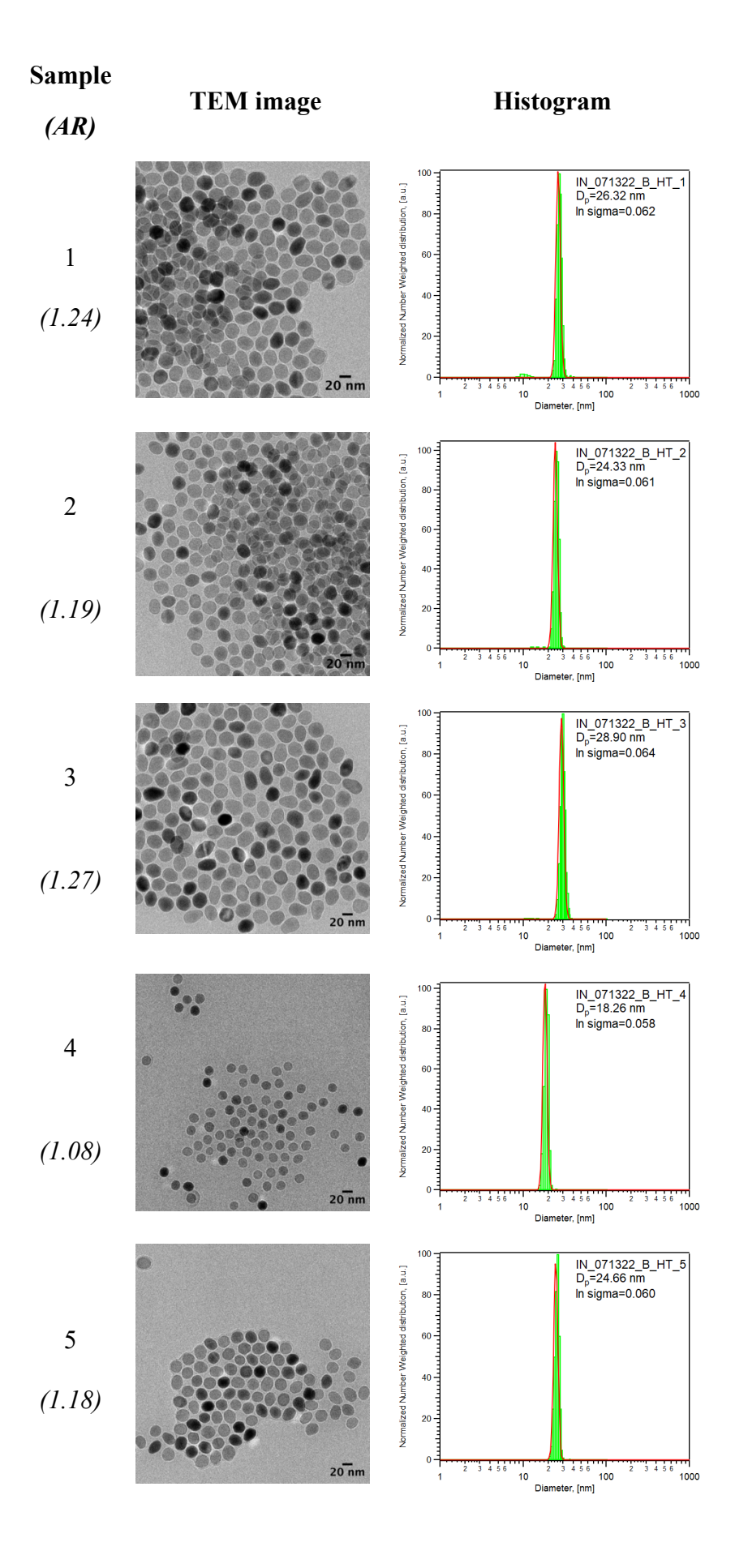


Figure S3. Representative TEM images and corresponding physical diameter distributions for all particles synthesized with a 3-hour post-synthesis treatment (PO3).



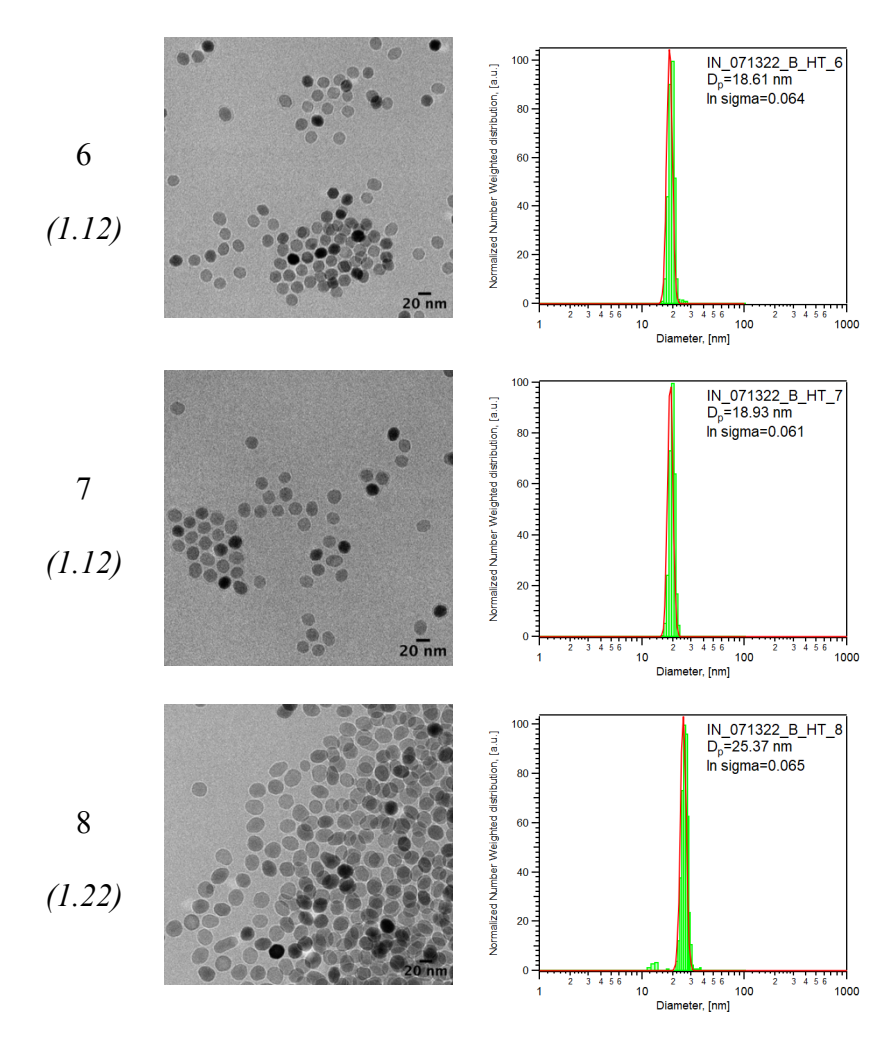
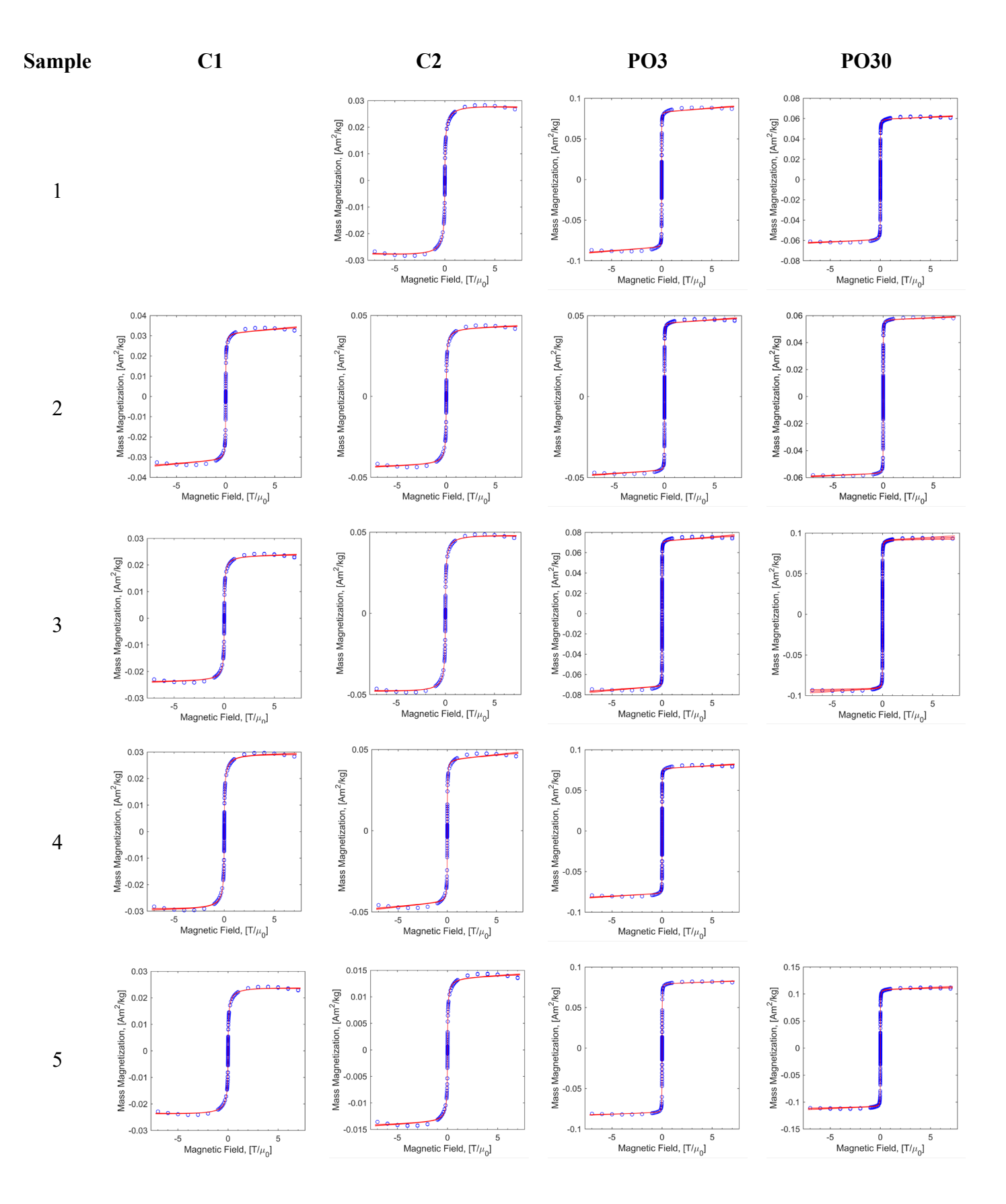


Figure S4. Representative TEM images and corresponding physical diameter distributions for all particles synthesized with a 30-hour post-synthesis treatment (PO30).



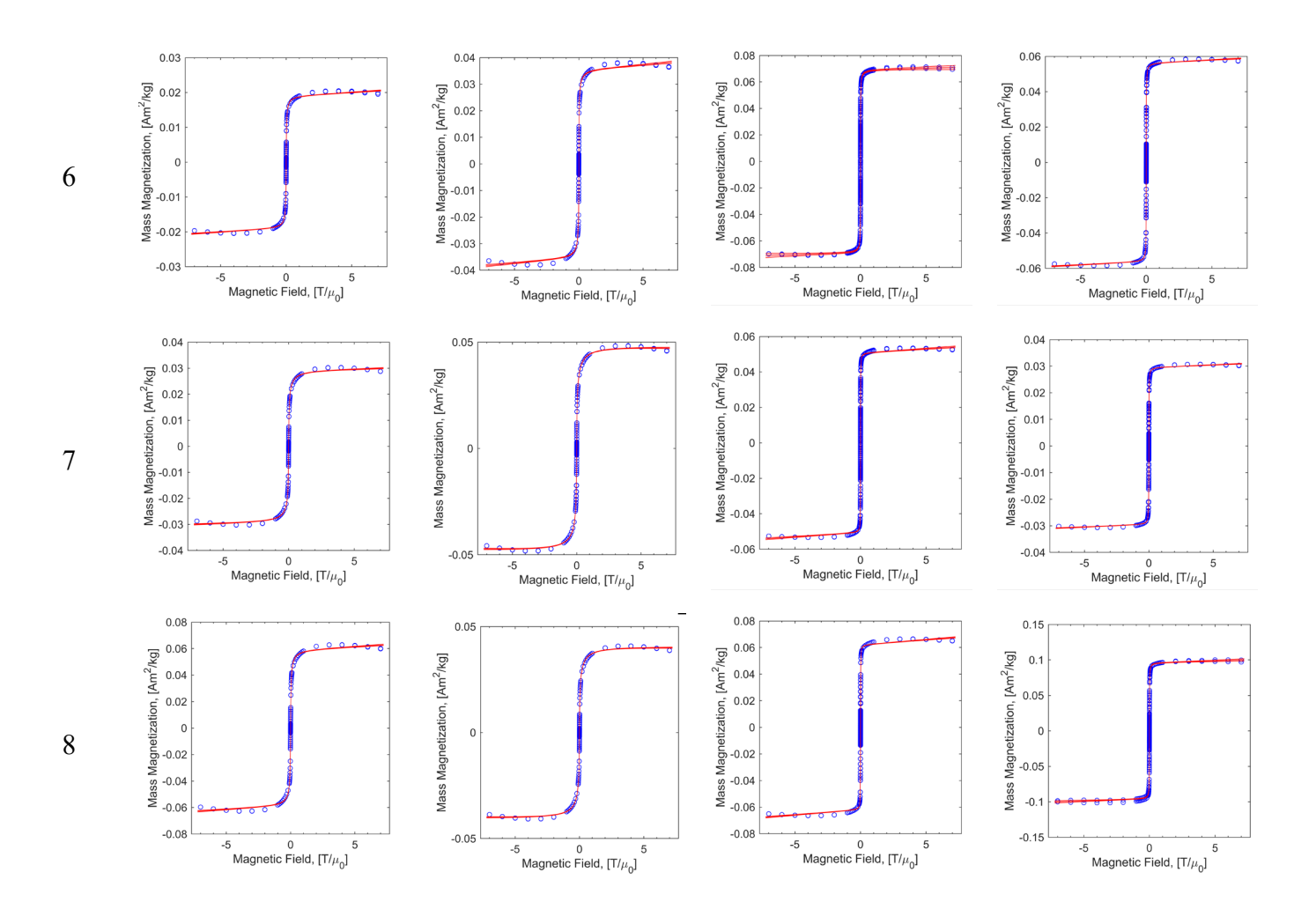


Figure S5. Magnetization (M) vs. magnetic field (H) curves at 300K of samples from groups C1, C2, PO3, and PO30 present superparamagnetic behavior.

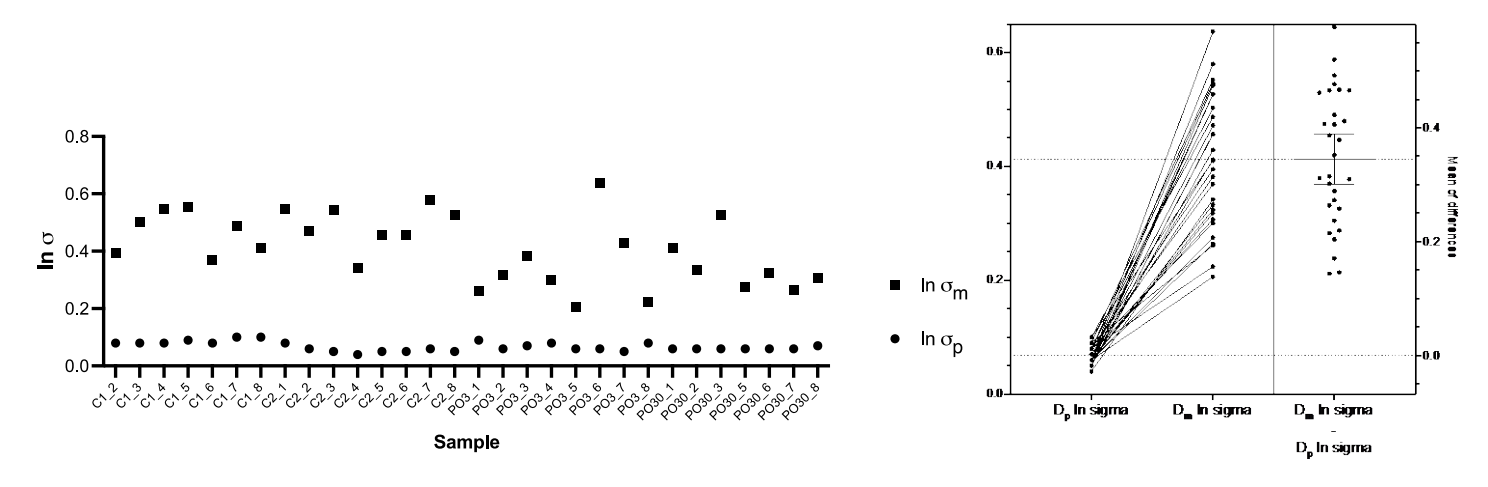


Figure S6. A paired t test of the geometric standard deviation of the physical diameter ($\ln \sigma_p$) and the magnetic diameter ($\ln \sigma_m$) of all samples in this study suggests larger variability in magnetic size compared to physical size.

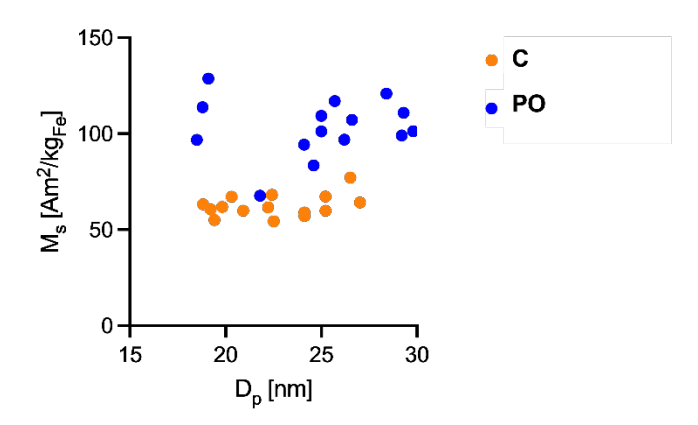


Figure S7. Dependence of saturation magnetization (M_s) on the nanoparticle physical diameter (D_p)

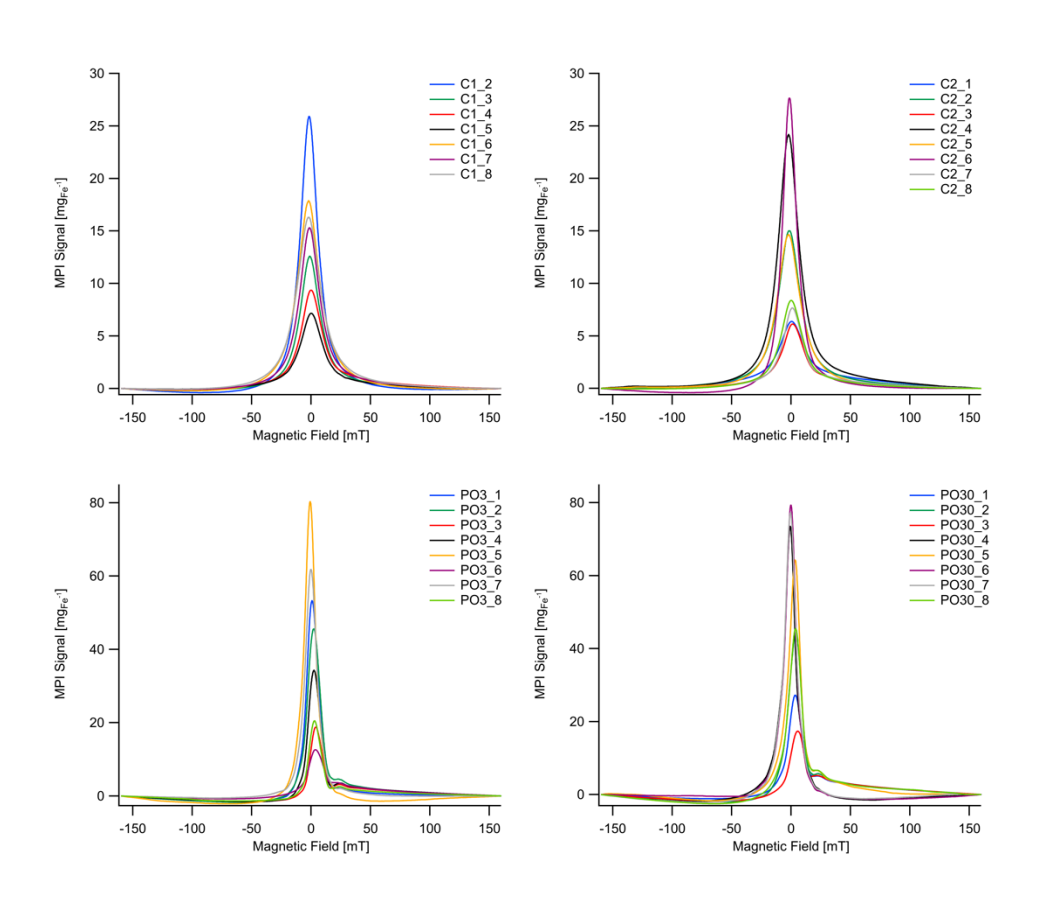


Figure S8. Point spread functions (PSF) obtained using the relax module in MOMENTUMTM scanner for all samples in the C1, C2, PO3, and PO30 groups.

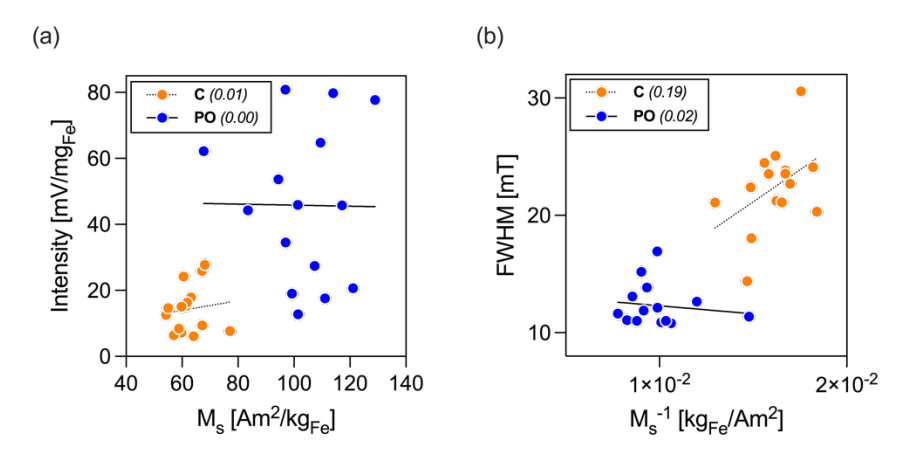


Figure S9. MPI performance correlations to the saturation magnetization (M_s) are very weak for both control and post-synthesis oxidation groups.

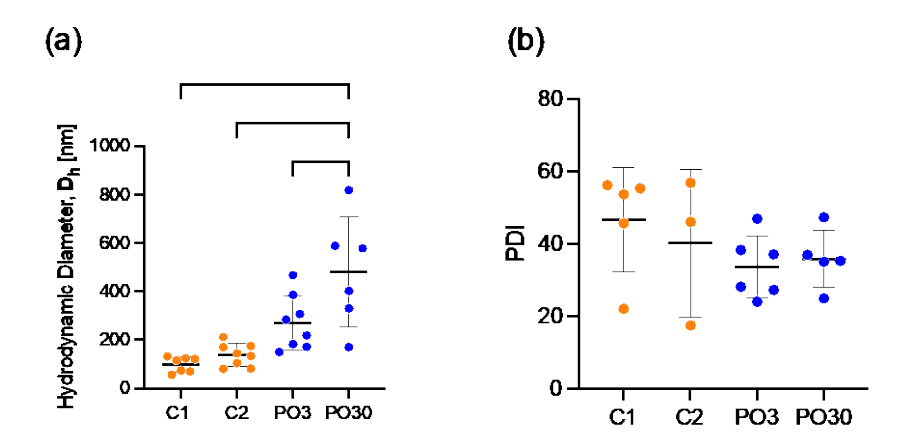


Figure S10. Hydrodynamic size evaluated via dynamic light scattering. (a) Effective hydrodynamic diameter (D_h) increases with post-synthesis oxidation, and (b) polydispersity index (PDI) remains consistent across synthesis conditions

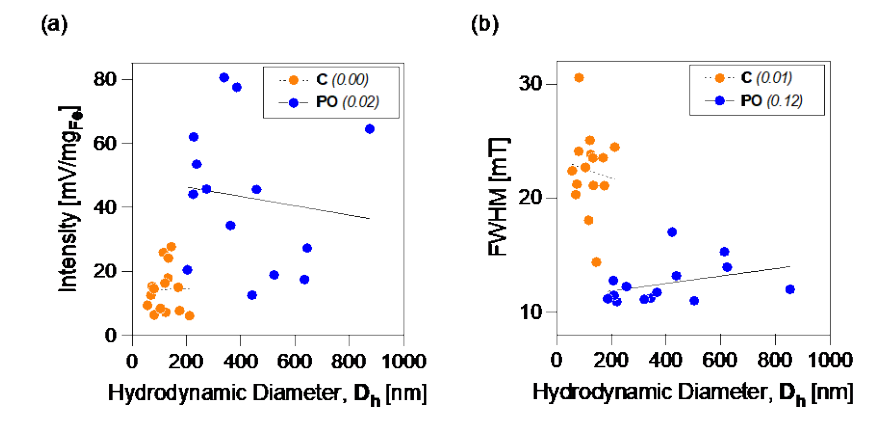


Figure S11. MPI performance correlations to the effective hydrodynamic diameter (D_h) are very weak for both control and post-synthesis oxidation groups.

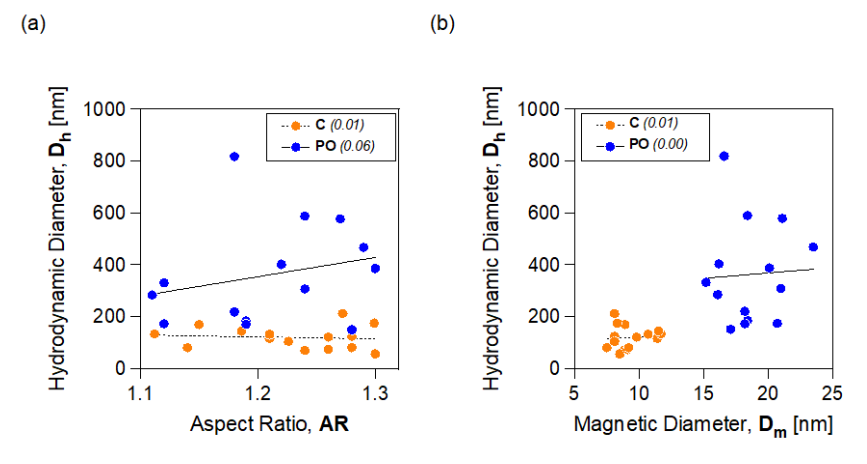


Figure S12. Effective hydrodynamic diameter (D_h) has no correlation to the nanoparticle (a) aspect ratio (AR) or (b) magnetic diameter (D_m) .

Table 1. Summary of nanoparticle properties measured or calculated for samples in each group: C1, C2, PO3, and PO30.

| Sample Name | Physical properties | | | | Magnetic | propertie | S | MPI performance | | | | |
|----------------|---------------------|-------------------|------|---------------------|-------------------|--------------------------------------|---|------------------------|--------------|-------------------------|-------------------------------|--|
| | D _p [nm] | ln σ _p | AR | D _m [nm] | ln σ _m | D _p - D _m [nm] | M _s [Am ² /kg _{Fe}] | Intensity [mV/mgFe] | FWHM [mT] | Pos. center offset [mT] | Neg. center offset [mT] | |
| C1_2 | 20.3 | 0.08 | 1.21 | 11.4 | 0.395 | 8.9 | 67.1 | 25.91 | 18.05 | -1.6 | 3.9 | |
| C1_3 | 22.5 | 0.08 | 1.24 | 8.8 | 0.503 | 13.7 | 54.3 | 12.59 | 20.3 | -0.7 | 3.1 | |
| C1_4 | 25.2 | 0.08 | 1.3 | 8.5 | 0.546 | 16.7 | 67.2 | 9.37 | 22.4 | 0.5 | 1.9 | |
| C1_5 | 25.2 | 0.09 | 1.28 | 8.1 | 0.552 | 17.1 | 59.8 | 7.16 | 23.82 | 0.4 | 1.9 | |
| C1_6 | 18.8 | 0.08 | 1.21 | 10.7 | 0.369 | 8.1 | 63.2 | 17.86 | 23.52 | -2 | 4.4 | |
| C1_7 | 22.2 | 0.1 | 1.26 | 9.1 | 0.487 | 13.1 | 61.6 | 15.3 | 21.23 | -1.1 | 3.5 | |
| C1_8 | 19.8 | 0.1 | 1.26 | 9.8 | 0.41 | 10 | 61.8 | 16.33 | 25.08 | -1.8 | 4.3 | |
| C2_1 | 24.1 | 0.08 | 1.28 | 7.5 | 0.546 | 16.6 | 57 | 6.38 | 30.57 | 1 | 1.6 | |
| C2_2 | 20.9 | 0.06 | 1.15 | 8.9 | 0.472 | 12 | 59.8 | 15.04 | 23.56 | -1.4 | 3.8 | |
| C2_3 | 27 | 0.05 | 1.27 | 8.1 | 0.542 | 18.9 | 64.1 | 6.14 | 24.46 | 1.8 | 0.7 | |
| C2_4 | 19.2 | 0.04 | 1.11 | 11.7 | 0.342 | 7.5 | 60.5 | 24.17 | 21.11 | -1.9 | 4.4 | |
| C2_5 | 19.4 | 0.05 | 1.14 | 9.2 | 0.456 | 10.2 | 55 | 14.65 | 24.1 | -1.9 | 4.3 | |
| C2_6 | 22.4 | 0.05 | 1.19 | 11.5 | 0.457 | 10.9 | 68.1 | 27.7 | 14.39 | -1.1 | 3.5 | |
| C2_7 | 26.5 | 0.06 | 1.30 | 8.3 | 0.58 | 18.2 | 77.1 | 7.7 | 21.09 | 1.5 | 0.9 | |
| C2_8 | 24.1 | 0.05 | 1.23 | 8.1 | 0.527 | 16 | 58.9 | 8.38 | 22.68 | 0.5 | 1.9 | |
| PO3_1 | 24.1 | 0.09 | 1.19 | 18.3 | 0.261 | 5.8 | 94.2 | 53.4 | 10.8 | 1.1 | 1.3 | |
| PO3_2 | 25 | 0.06 | 1.18 | 18.1 | 0.318 | 6.9 | 101.1 | 45.63 | 12.13 | 2.4 | 0 | |

| PO3_3 | 29.2 | 0.07 | 1.29 | 23.4 | 0.382 | 5.8 | 99 | 18.85 | 10.88 | 4.5 | -2.1 |
|--------|------|------|------|------|-------|------|-------|-------|-------|------|------|
| PO3_4 | 26.2 | 0.08 | 1.24 | 20.9 | 0.3 | 5.3 | 96.8 | 34.31 | 11.11 | 2.8 | -0.4 |
| PO3_5 | 18.5 | 0.06 | 1.11 | 16 | 0.206 | 2.5 | 96.7 | 80.4 | 11 | -0.9 | 3.3 |
| PO3_6 | 29.8 | 0.06 | 1.30 | 20 | 0.637 | 9.8 | 101.2 | 12.64 | 16.92 | 4.8 | -2.2 |
| PO3_7 | 21.8 | 0.05 | 1.12 | 20.6 | 0.429 | 1.2 | 67.6 | 61.89 | 11.37 | 0 | 2.4 |
| PO3_8 | 28.4 | 0.08 | 1.28 | 17 | 0.224 | 11.4 | 120.8 | 20.52 | 11.07 | 3.4 | -1 |
| PO30_1 | 26.6 | 0.06 | 1.24 | 18.3 | 0.412 | 8.3 | 107.1 | 27.24 | 13.85 | 3.9 | -1.4 |
| PO30_2 | 24.6 | 0.06 | 1.19 | 18.1 | 0.333 | 6.5 | 83.4 | 44.05 | 12.65 | 3.5 | -1.1 |
| PO30_3 | 29.3 | 0.06 | 1.27 | 21 | 0.527 | 8.3 | 110.8 | 17.45 | 15.18 | 6 | -3.8 |
| PO30_5 | 25 | 0.06 | 1.18 | 16.5 | 0.275 | 8.5 | 109.2 | 64.4 | 11.88 | 2.9 | -0.5 |
| PO30_6 | 18.8 | 0.06 | 1.12 | 15.5 | 0.324 | 3.3 | 113.7 | 79.4 | 11 | -0.5 | 2.9 |
| PO30_7 | 19.1 | 0.06 | 1.12 | 15.1 | 0.264 | 4 | 128.6 | 77.3 | 11.63 | -0.7 | 3.1 |
| PO30_8 | 25.7 | 0.07 | 1.22 | 16.1 | 0.307 | 9.6 | 116.9 | 45.52 | 13.1 | 3.6 | -1.1 |